Rheological characterization of weakly rate-thickening automotive oils through an improved Capillary Breakup Extensional Rheometer (CaBER)

Jianyi Du[a], Hiroko Ohtani[b], Crystal E. Owens[a], Lenan Zhang[a], Kevin Ellwood[b], Gareth H. McKinley[a,*]

[a]*Department of Mechanical Engineering, Massachusetts Institute of Technology, 77 Massachusetts Ave, Cambridge, MA 02139, USA*
[b]*Vehicle Manufacturing and Additive Manufacturing-Metals, Ford Motor Company, Dearborn, MI 48121, USA*

Abstract

We describe a customized Capillary Breakup Extensional Rheometer (CaBER) with improved dynamic performance and added features for temperature control over the range from room temperature up to 250°C. The system is aimed at characterizing the extensional rheological behavior of weakly rate-thickening fluids that are widely utilized in the automotive industry. We examine the shear rheology and filament-thinning dynamics of two commercially available automotive fluids with the same viscosity index. Comparisons of the rheological properties of the two samples reveal that although they have identical shear viscosities, they exhibit significant and distinct rate-thickening behavior in the strong extensional flow that is generated close to filament breakup. For the more elastic sample, the exponential filament-thinning dynamics are well-described by the Oldroyd-B model; however, this viscoelastic model poorly describes the response of the more weakly rate-thickening fluid. To address this limitation, we propose a simple Inelastic Rate-Thickening (IRT) model that more robustly describes the measured material response. The two constitutive parameters of the model represent the zero-shear-rate viscosity of the fluid and the rate of extensional thickening in the fluid. Numerical calculations with the IRT model show that the radii of thinning fluid filaments deviate from a linear decay in time and approach a quadratic dependence very close to break up. By carefully fitting the measured temporal evolution in the mid-plane radius we can therefore systematically differentiate the extensional rheological response of the two oils. More generally, we show that the weakly rate-thickening regime can be distinguished from the well-known elasto-capillary response predicted by the Oldroyd-B model, via a constraint on the relaxation time (or more specifically the elasto-capillary number) of the fluid. The weakly rate-thickening behavior documented in these oils is representative of the extensional rheology of many industrial fluids at large extensional strain rates ($100\text{-}1000\text{s}^{-1}$) and is important in many industrial processes such as jetting, coating and stamping.

Keywords: automotive oils, weakly rate-thickening fluids, extensional rheology, CaBER

---

*Corresponding author (gareth@mit.edu)

1. Introduction

Lubricating oils, or engine oils, find extensive applications in the manufacturing and automotive fields, as well as in most vehicles to reduce friction and wear. Generally composed of alkane-based components refined from crude oil, different grades of motor oils can be obtained by altering the purity of refinement or adjusting the chain length and the relative concentrations of different alkane components in the blended oil [1]. The variety of commercial lubricating oil products is further expanded by a number of additives, which enhance specific features such as improved lubrication, thermal stability, oxidation inhibition, anti-corrosion, and chemical resistance [2]. The search for new additives in this dynamic field is an ongoing topic across multiple industries as well as in academia [3]. The primary focus is on discovering novel materials and formulations in order to optimize the performance or to integrate desired properties for specific purposes [2, 4]. These lubricating oil additives cover a wide range of material systems, including polymers [5], zinc dithiophosphate (ZDDP) [6, 7, 8] or other metal compounds [3], micro- or nanoparticles [9, 10, 11], antioxidants [3, 12, 13] and surfactants [14].

Besides the variety of chemical components that leads to the large number of lubricating oils available, there are additional factors arising from the operating environment (pressure, temperature, humidity, electric or magnetic field) and the flow field (strain or strain rate) that can impact the effective fluid properties [3, 15], flow instabilities [16], and flow assurance [17]. In most industrial scenarios, the working conditions are expected to be extreme, and the fluid properties become increasingly susceptible to environmental variations. To understand these variations and to minimize service life reduction or damage to the operating hardware [15], it is essential to have a complete knowledge of the fluid rheological properties.

Lubricating oils are standardized based on the kinematic viscosities at specific temperatures through familiar categories such as 10W-30, 10W-40 and 20W-50 [1]. A large number of previous rheological studies on commercial motor oils have demonstrated Newtonian behavior in steady shear flows, supporting the choice of using a single reported viscosity as a suitable metric [1, 15]. Over the past few decades, however, the increasing demands on lubricant capabilities have driven the development of additive packages that can tune the rheology to various working conditions [3]. This concomitantly brings potential modifications to the fluid properties that are not captured in the SAE standards [1]. The aforementioned additives including polymers or nanoparticles can substantially alter the rheological properties of the product as a result of hydrodynamic interactions between the different components and new contributions to the total stress that arises from the additive phases [18]. It is now well-understood that the rheology of various dispersion systems such as particle suspensions [19, 20], emulsions [21] and polymer solutions [22, 23] can be substantially modified even at low concentrations of the dispersed phase, but the consequence on the rheology of lubricant systems have not been considered in depth. Moreover, the bulk rheological properties of a complex material system will vary with the kinematics of the flow field. In particular, common flow scenarios for motor oils combine both

shear and extensional components (e.g. flows in converging pipes and ducts, jet impingement and atomization) [24]. In a strong extensional flow, substantial changes in the lubricant rheology may arise from flow-induced anisotropy, particle jamming, strain-hardening of the dispersed polymer chains, or other microstructural variations [18, 25, 22]. These complexities can drive significant modifications to the lubricant performance, such as changes in lubricant film thickness due to oil elasticity [26], or the need for higher-order corrections in lubrication models commonly used in automotive applications [27]. As a consequence, more detailed rheological characterization is required for advanced lubricating formulations to account for their increasingly sophisticated industrial applications.

In this paper, the extensional rheology of two commercially available motor oils is investigated. A customized Capillary Breakup Extensional Rheometer (CaBER) based on the familiar capillary thinning technique is constructed with improved performance and added features (e.g. temperature control and faster motor actuation) specifically for industrial fluid measurements. Capillary thinning measurements on the two motor oils show substantial deviations from the Newtonian predictions at high strain rates, indicating rate-thickening phenomena in a strong extensional flow. However, we show that the elasto-capillary balance expected from the familiar Oldroyd-B model is only appropriate for describing the rheological behavior of the more elastic sample. To address this limitation, we propose a simple Inelastic Rate-Thickening (IRT) model that can quantify the rheological response of more weakly rate-thickening fluids. This leads to a practical and data-rich framework for extensional rheological characterizations of both weakly and strongly rate-thickening materials, which are commonly encountered in industrial applications.

2. Experimental setup and materials

2.1. Customized capillary thinning system

The capillary breakup technique provides a method to measure the transient extensional rheology of complex fluids with low and moderate viscosity. Based on the dynamics of liquid filament thinning, the Liquid Filament Microrheometer was first introduced by Bazilevsky et al. [28], and has been developed into the modern Capillary Extensional Breakup Rheometer (CaBER) as a robust and widespread technique [25]. As the schematic illustrates in Fig. 1, the capillary thinning technique works by rapidly stretching a cylindrical liquid sample between two coaxial discs with diameter $2R_0$ and initial gap L_0 to a final separation L_f in the axial direction, using a fast axial strain (actuation time typically less than 50ms). During the dynamic capillarity-driven process of fluid pinch-off into two separate drops, a transient liquid filament forms and the radial profile of the liquid bridge is a function of time and the axial position, $R = R(z, t)$. The structural evolution of the liquid filament is a self-thinning process driven by surface tension and resisted by the viscosity and elasticity of the liquid. In the absence of gravity, the temporal evolution of the mid-plane radius of the liquid bridge $R_{mid}(t) = R(0, t)$ captures these self-thinning dynamics and can be used to extract a measure of the transient extensional rheological properties of an unknown material.
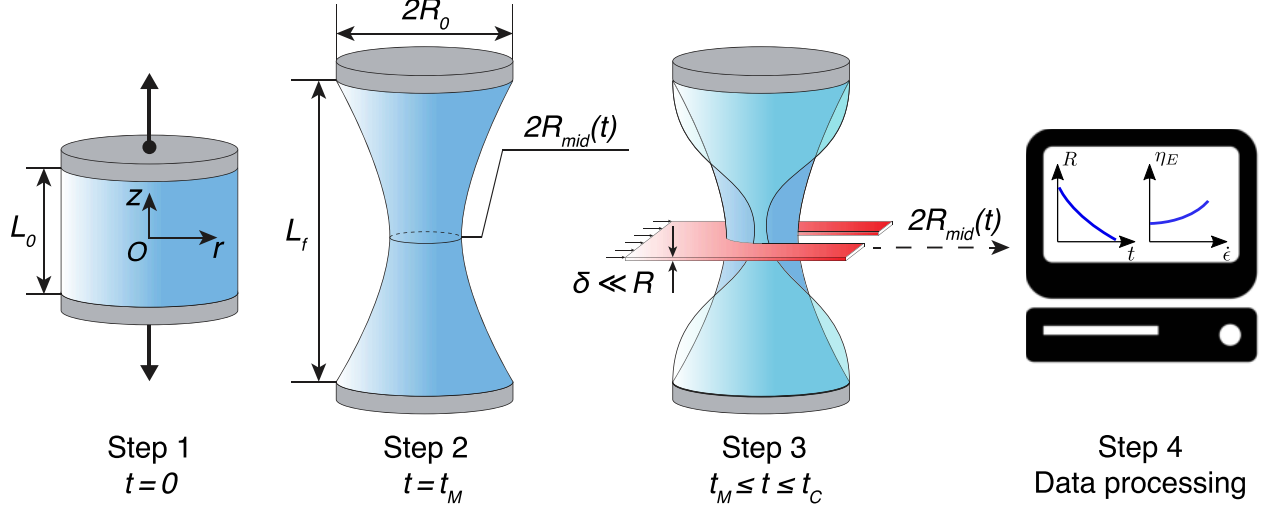
3

Figure 1: Schematic of the capillary thinning experiment. The system is initialized in Step 1 ($t = 0$) with a cylindrical sample volume placed between two discs with diameter $2R_0$ and an initial separation gap of L_0. The two discs actuate to stretch the sample axially in a quasi-step strain manner to the final gap L_f within time t_M. Step 2 at $t = t_M$ indicates the time at which the two discs stop moving. After this time, the liquid bridge formed between the two discs goes through a self-thinning process governed by visco-elasto-capillary interactions until it breaks up at time t_C, as shown in Step 3. The temporal evolution quantified by the mid-plane radius $R_{mid}(t) = R(0, t)$ is recorded by an optical device, such as a laser micrometer or a high-speed camera. In Step 4, the filament thinning data are further processed to extract the material properties of the sample given the selection of a suitable constitutive model.

The signature of this thinning process must be captured by the appropriate constitutive model. In the simplest description, the liquid bridge is treated as a one-dimensional model and is assumed to remain cylindrical during deformation. The radius of the liquid bridge $R(t)$ then becomes independent of the axial z position. The resulting extensional flow can be characterized by a specific form of the strain rate tensor $\dot{\boldsymbol{\gamma}}$ as

$$\dot{\boldsymbol{\gamma}} = \begin{bmatrix} -\dot{\epsilon} & 0 & 0 \\ 0 & -\dot{\epsilon} & 0 \\ 0 & 0 & 2\dot{\epsilon} \end{bmatrix}, \tag{1}$$

where the extension rate $\dot{\epsilon}(t) = -2\dot{R}_{mid}(t)/R_{mid}(t)$ is a function of time t. In practice, however, the curvature of the liquid bridge in the axial direction is not always negligible even at the midpoint. The resulting filament profile $R(z, t)$ varies both spatially (z) and temporally (t). In the case of slender-shaped liquid bridges, Renardy [29] derived a "1+1" dimensional Lagrangian formulation to describe the filament thinning. With this formulation, McKinley and Tripathi [30] rewrote the stress balance equation for the filament in terms of the net axial force term $F_e(t)$ acting on a control volume as

$$\eta_E^+ \dot{\epsilon} = 3\eta_S\dot{\epsilon} + \Delta\sigma^{nN} = \frac{F_e(t)}{\pi R^2} - \Delta p_c, \tag{2}$$

where η_E^+ is the total transient extensional viscosity and it is decomposed into a solvent term $3\eta_S\dot{\epsilon}$ and a non-Newtonian

4

contribution $\Delta\sigma^{nN}(\dot{\epsilon}, t) = \sigma_{zz}^{nN} - \sigma_{rr}^{nN}$. The term Δp_c is the capillary pressure, which can be expressed using the Young-Laplace equation [31] as

$$\Delta p_c = \frac{\Gamma}{R}\left[\frac{1}{(1 + R'^2)^{1/2}} + \frac{RR''}{(1 + R'^2)^{3/2}}\right], \tag{3}$$

where $R' = \partial R/\partial z$ and $R'' = \partial^2 R/\partial z^2$.

Using a control volume analysis, the external axial force $F_e(t)$ can be viewed as being exerted by the stationary reservoir of fluid on the liquid bridge and originates from the capillarity of the liquid bridge. As a result, dimensional analysis indicates that $F_e(t)$ scales with $2\pi\Gamma R_{mid}(t)$, where Γ is the surface tension of the fluid. We follow the notation of [30] to let $F_e(t) = 2\pi X\Gamma R_{mid}(t)$, where $X(t)$ is a geometric correction factor which may vary with time to incorporate the non-cylindrical liquid profile shape. Eq. (2) is based on the assumptions of negligible gravitational effects (Bond number $Bo = \rho g R^2/\Gamma \ll 1$) and also negligible inertial effects (Ohnesorge number $Oh = \eta_0/\sqrt{\rho\Gamma R_0} \gtrsim O(1)$) [30]. When an appropriate viscoelastic constitutive model is specified, the temporal evolution of $R_{mid}(t)$ can be obtained by solving Eqs. (1)-(3) in conjunction with the evolution equations for σ_{zz}^{nN} and σ_{rr}^{nN}. As a result, the underlying material properties can be extracted from obtaining the dynamics of $R_{mid}(t)$. Over the past few decades, explicit solutions of $R_{mid}(t)$ from Eqs. (1)-(3) have been obtained for various constitutive models ranging from the Newtonian fluid [29, 30, 32] to a series of viscoelastic fluids [25, 29]. Recent studies have investigated more complex material systems including yield-stress fluids [33, 34, 35], emulsions [33] and particulate suspensions [36, 37, 38].

(a) Motor

(b) Laser micrometer

(c) Heating modules

(d) Chamber and backlight
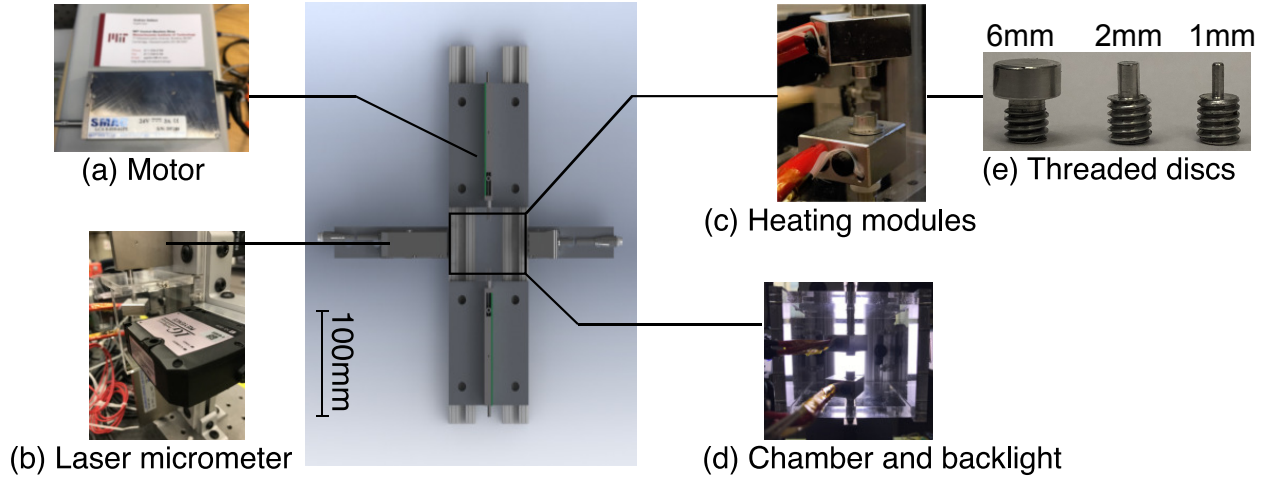
(e) Threaded discs

6mm   2mm   1mm

100mm

Figure 2: Schematic and images of the customized CaBER system. The scale bar is 100mm. The system is comprised of four primary components mounted on an 80/20 aluminum extrusion framework. (a) Two identical linear actuators drive each disc separately, with a maximum stroke of 10mm for each, in an actuation time under 30ms. (b) The laser micrometer is positioned close to the mid-plane and is used to measure the mid-plane radius $R_{mid}(t)$, with a minimum detectable object size 100μm in diameter and a resolution of 5μm. (c) The resistance heating modules installed beneath the discs can maintain a temperature of up to $250°$C with a precision of $\pm1°$C. (d) The acrylic chamber is manufactured by laser cutting to isolate samples in controlled environmental conditions. (e) The customized aluminum discs have threads to allow easy exchange on the heating modules. A series of plate diameter options allow multipurpose measurements using the same instrument.

In addition to CaBER, a number of other extensional rheometers based on filament thinning techniques are available. Examples include the liquid filament microrheometer [28] and the free-jet elongational rheometer [39]. In more recent studies, the Rayleigh-Ohnesorge Jetting Extensional Rheometer (ROJER) [40] and dripping-on-substrate devices (DOS) [41] have allowed the characterization of extensional rheology for liquids with lower viscosities and smaller relaxation times. In this work, a customized CaBER system is constructed in accord with the need to characterize various lubricating oils utilized in industry. This choice is made for three reasons: ease of use for a wide range of liquid viscosities, capability of environmental control, as well as integration with more advanced capillary thinning techniques. According to the SAE standards [1], the kinematic viscosities of common lubricating oils range from 10^{-5} to $10^{-2} \mathrm{m}^2/\mathrm{s}$ in most industrial applications. Almost this entire viscosity range is accessible with the operating regime of CaBER [42]. Compared with other capillary thinning techniques, the CaBER system is easier to operate, less costly with fewer components, and requires the least amount of sample for a single test ($\sim 60\mu$L), while a number of extensional rheological properties (eg. the time to breakup and the apparent extensional viscosity) can be extracted easily with high accuracy. Furthermore, a customized CaBER system allows for additional environmental control or integration of optical probes to investigate the extensional rheology of lubricating oils at different operating temperatures or relative humidities. Finally, a customized CaBER system also allows for the programming of motor motion with user-defined speeds, accelerations, and even displacement-time profiles. This feature enables the system to also perform additional more advanced experimental protocols such as the Slow Retraction Method, which can probe the extensional rheology of liquids with lower viscosities (down to approximately $30\mathrm{mPa} \cdot \mathrm{s}$) [43].

Fig. 2 shows the assembly and individual components of the customized CaBER system. The main components of this system include (i) two business card-sized linear servo motors (LCA8-010, SMAC Moving Coil Actuators Inc.) which serve as symmetric actuators with a maximum displacement, or full stroke, of 10mm for each motor; (ii) a multi-purpose charged-coupled device (CCD) laser micrometer with a minimum object size of 100μm in diameter and resolution of 5μm (IG-028, amplified with IG-1000, Keyence Corp); (iii) a high-speed imaging system (Phantom M320s, Vision Research Inc.) with a frame rate of 4000fps (or higher) for an observation window size of 500px$\times$700px and an image resolution of 17μm/px (the resolution can be further improved with a macro lens of higher magnification); (iv) a backlighting system to enhance the exposure for high speed imaging (IR Backlight, Phlox Inc.) with size of 40mm $\times$ 40mm and a luminous flux of approximately 530lumens; (v) two commercial resistance heating modules with resistance temperature detectors (RTD) controlled by pulse width modulation (PWM), with maximum attainable temperature of 250°C and an accuracy of $\pm$1°C; (vi) two interchangeable threaded aluminum discs to hold the liquid samples; (vii) customized 80/20 aluminum t-slotted extrusion frame; (viii) the hardware I/O interface (NI 6002, National Instruments), communicated through a customized user interface programmed in LabVIEW (National Instruments). The necessary calibrations and preliminary tests of these components have been performed [44] and the results are summarized in Appendix A.

2.2. Materials and preliminary characterizations

   Two representative synthetic motor oils are chosen for detailed study in this work: Castrol High-Mileage Synthetic

Blends (denoted as CSB; Castrol, Naperville, IL) and Mobil 1 (denoted as M1; ExxonMobil, Spring, TX). Both oils

are graded 10W-30 according to the SAE standards [1]. From the standards, the viscosity indices (VI) of both oils are

calculated (CSB: 138.1; M1: 146.0) and found to be close to each other. The equivalency of this VI rating indicates that

both oils have similar shear viscosities at the same temperature. As shown in Table 1, independent characterization

of the shear rheology (DHR-3, TA Instruments) and surface tension (DCAT, dataphysics) are performed at room

temperature (25°C). The shear viscosities of both oils from shear rheometry are rate-independent and only differ from

each other by 8%. Using these measurements, we can calculate that for discs with radius $R_0 = 3$mm, the Ohnesorge

number during capillary thinning is $Oh \gtrsim 0.5$. Since we have $Oh \sim O(1)$, we expect a visco-capillary (VC) balance

during the filament thinning process and the VC thinning timescale can be used as an *a priori* measure of the time to

breakup; $t_{VC} \sim (\eta_0 R_0)/\Gamma \approx 17$ms. These two oils can thus act as model materials to produce distinct capillary thinning

phenomena and their extensional rheology can be extracted from the CaBER system.

Table 1: Independent shear rheological characterization and surface tension measurements of the two commercial motor oils. From shear rheometry alone, we conclude that both materials are Newtonian with rate-independent shear viscosities up to $\dot{\gamma} = 1000$s^{-1}. Both Ohnesorge numbers are on the order of unity and will result in dominant visco-capillary thinning profiles. The Bond number Bo based on the disc radius R_0 is greater than unity; however, gravitational effects become almost negligible in the final stage of breakup when $R(t) \ll R_0$. More details are shown in Section 3.

	Viscosity Index (VI)	η_0[Pa $\cdot$ s]	Γ[mN/m]	$Oh = \eta_0/\sqrt{\rho\Gamma R_0}$	$Bo_0 = \rho g R_0^2/\Gamma$
CSB	138.1	0.132 ± 0.002	23.10 ± 0.02	0.54	3.29
M1	146.0	0.142 ± 0.001	24.80 ± 0.01	0.56	3.07

3. Results and discussions

   The extensional rheology of both motor oils have been investigated using our customized CaBER system. The

experimental parameters characterizing the measurements are listed in Table 2. Fig. 3 shows snapshots of the liquid

filament profiles from high-speed imaging. All snapshots are timestamped according to the notation shown in Fig. 1.

From Fig. 3, it is clear that two distinct regions of filament evolution can be distinguished. In Region 1 ($t \lesssim 90$ms), the

liquid bridges of both oils are aligned at identical timestamps, and they share a similar wineglass-stem shape. In this

regime, both axial and radial curvature terms described by Eq. (3) play a role in the evolution of the liquid filament.

In Region 2 ($t \gtrsim 90$ms), the profiles of both liquid bridges become progressively more slender and they also steadily

deviate from each other in shape. The resulting breakup time t_C is thus different for the two oils (CSB: $t_C \approx 123$ms;

M1: $t_C \approx 108$ms).

Table 2: Experimental parameters of the customized CaBER system for capillary thinning tests on the two sample oils.

Parameters	Values
Disc diameter $2R_0$	6.0mm
Ambient temperature	$25 \pm 0.5°C$
Motor actuation time t_M	30ms
Initial gap L_0	2.0mm
Final gap L_f	7.7mm
Hencky strain ϵ	1.35
High-speed camera frame rate	6700fps
Resolution	$17\mu m/px$

(a)

(b)

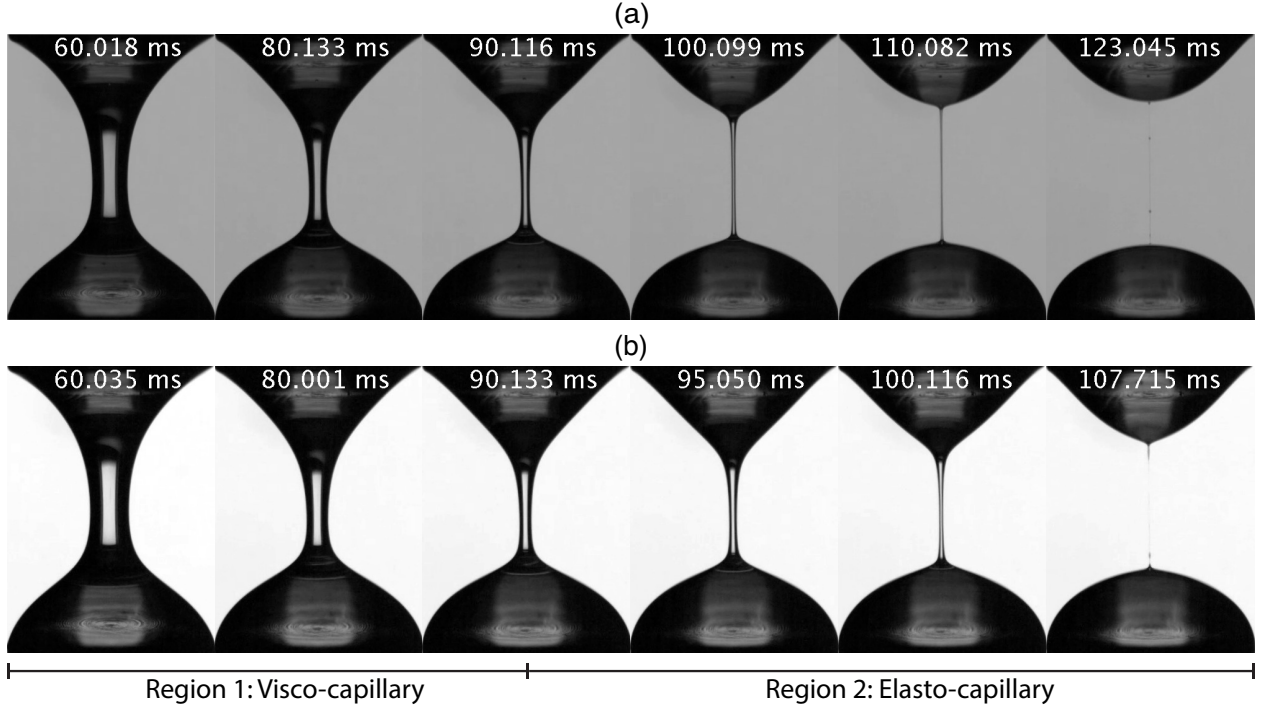Region 1: Visco-capillary   Region 2: Elasto-capillary

Figure 3: Snapshots of the thinning profiles of two motor oils tested on the customized CaBER system: (a) Castrol High-Mileage Synthetic Blend (CSB). (b) Mobil 1 (M1). The experimental parameters are listed in Table 2, with the elapsed time t marked in the figures. Detailed comparison of the two subfigures shows that the liquid bridges formed between the two end reservoirs are very similar in shape at $t \lesssim 90$ms. The profiles differ increasingly beyond $t \approx 90$ms as the liquid bridges become increasingly slender, the strain rate increases, and this finally results in distinct breakup times.

To better demonstrate the evolution of liquid bridges during the capillary thinning process, we extract the evolving free surface profiles of both oils $R(z,t)$ from Fig. 3 using an edge detection routine, and the results are plotted in Fig. 4(a) and (b). In both subfigures, the regions within a distance of one capillary length ($l_{cap} = \sqrt{\Gamma/\rho g} \sim 1.5$mm) from each disc are marked in gray. In these quasistatic regions, the shapes of the liquid reservoirs are primarily governed by the interaction between gravitational and capillary effects, and capillary thinning dynamics do not apply. When $t \lesssim 90$ms, the liquid profiles of both oils $R(z,t)$ are similar and resemble the classical results of Papageorgiou [32] in the form of a curved, self-similar shape which is skewed slightly by the symmetry-breaking effects of gravity.

140 However, as the filament profiles of both oils become progressively slender (90ms $\lesssim t \lesssim t_C$), their shapes increasingly deviate from each other. As shown in Fig. 3, the CSB oil evolves into a nearly cylindrical profile at $t \gtrsim$ 110ms with a sharp axial transition between the thinning liquid filament and the quasi-static reservoirs at each end plate, while the M1 oil maintains a more curved profile until finally pinching off at $t_C \approx$ 108ms.
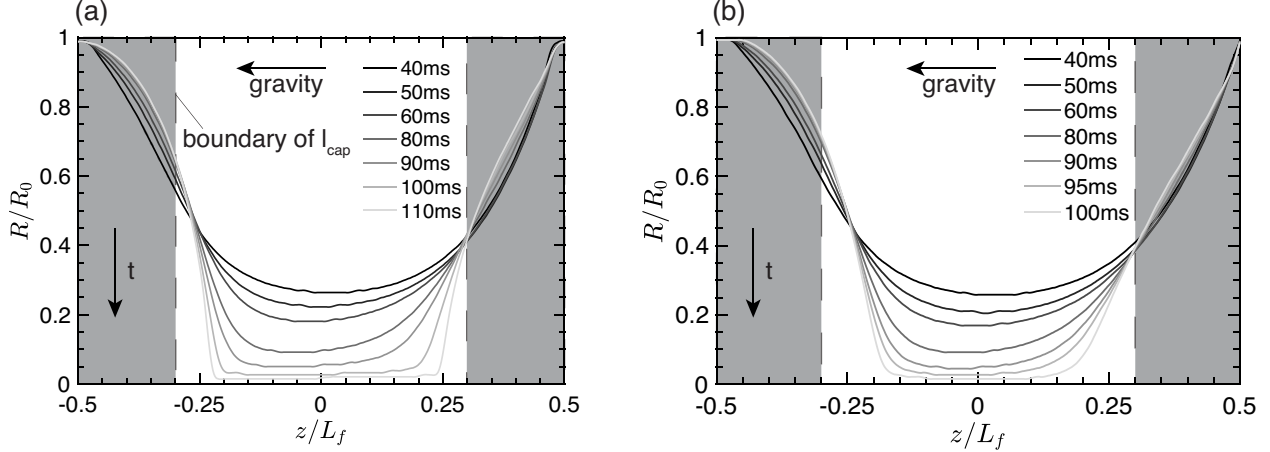

Figure 4: Liquid bridge profiles at different time for both oils, extracted from the video snapshots in Fig. 3. (a) The CSB oil at times t = 40ms, 50ms, 60ms, 80ms, 90ms, 100ms and 110ms. (b) The M1 oil at times t = 40ms, 50ms, 60ms, 80ms, 90ms, 95ms, 100ms. In both figures, $|z/L_f|$ = 0.5 corresponds to the positions of the upper and lower disc, and the gray-shaded regions with $|z/L_f| \gtrsim 0.3$ are within one capillary length l_{cap} from each stationary end disc, which serves to stabilize the thinning liquid bridge [25].

From Fig. 4, the evolution of the liquid profiles for both oils can be conveniently summarized using the minimum filament diameter $D(t)$ defined as

$$D(t) = \min_{-\frac{L_f}{2} \leq z \leq \frac{L_f}{2}} [2R(z, t)]. \tag{4}$$

We extract $D(t)$ for both oils from the snapshots in Fig. 3, and the results are shown in Fig. 5(a). Careful comparison with Fig. 3 shows that the temporal evolution of $D(t)$ captures the key features of the filament profiles: For $40 \lesssim t \lesssim$ 90ms (Region 1 in Fig. 3), the filament diameter $D(t)$ decays linearly with time for both oils. This linear evolution is consistent with the capillary thinning dynamics of Newtonian fluid filaments governed by a VC balance. The corresponding filament diameter for a Newtonian fluid can be expressed as [30]

$$D^N(t) = 0.1418 \frac{\Gamma}{\eta_0} (t_C - t), \tag{5}$$

where η_0 is the Newtonian viscosity. By fitting Eq. (5) to this linear-thinning region ($t \geq t_M \approx$ 35ms) in Fig. 5(a), we obtain the dotted line. From the slope, the shear viscosities can be determined experimentally (with Γ known). The results are shown in Table 3 and are close to the independent measurements from shear rheometry (Table 1). In addition, extrapolation of the linear prediction from the Newtonian-fluid model leads to a breakup time of $t_C^N \approx$ 100ms
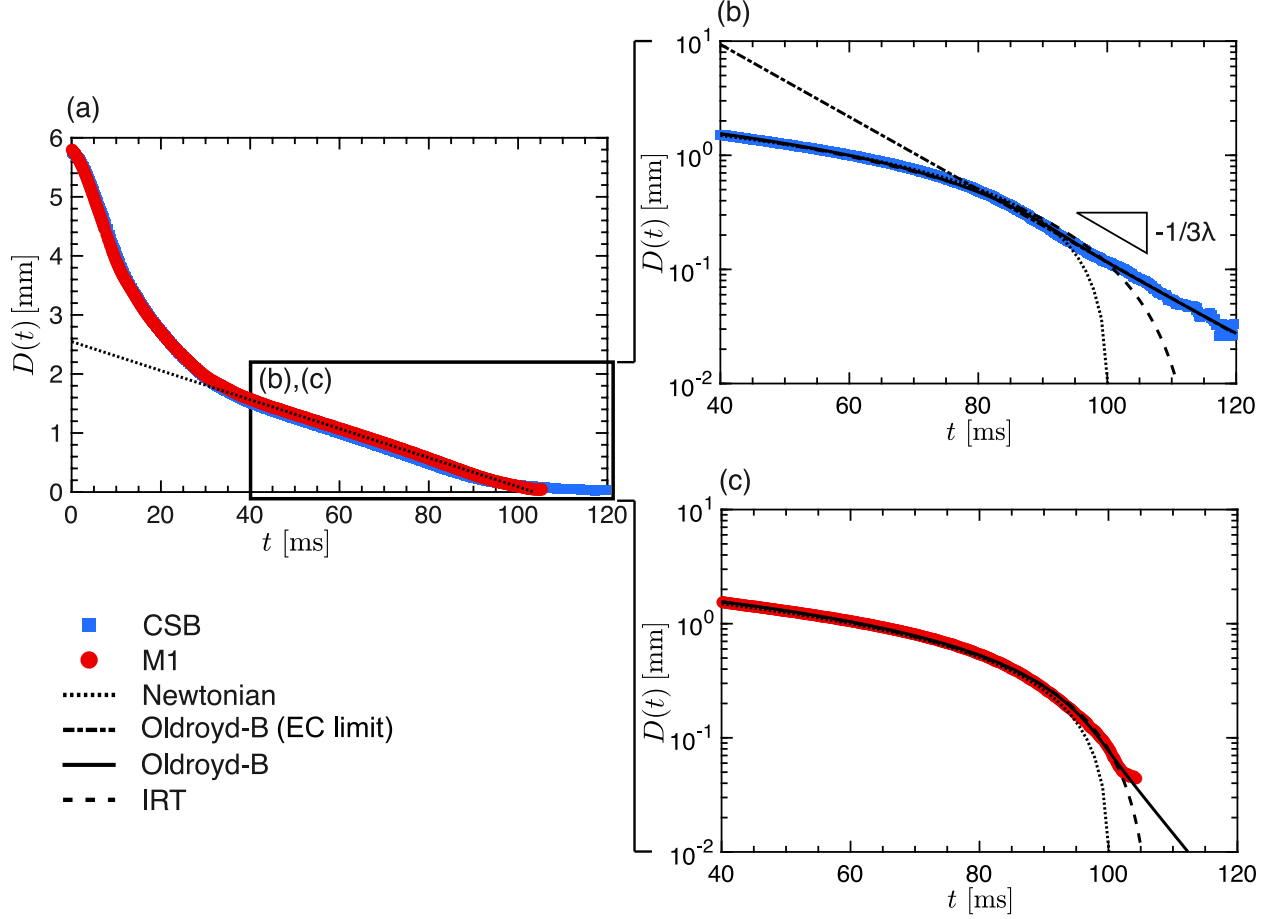
9

Figure 5: Evolution in the minimum filament diameter $D(t)$ extracted from high-speed imaging of capillary thinning for the two motor oils. The experimental parameters are given in Table 2. (a) Linear-linear plot. Overlapping linear VC thinning regimes are observed for both motor oils between 40ms$\lesssim t \lesssim$ 90ms and can be fit by the Newtonian fluid model (dotted line). (b) and (c) show enlarged views with a logarithmic ordinate between 40ms$< t <$ 120ms. The Newtonian (linear) fitting is valid till $t \approx$ 90ms, and the exponential thinning regime of the CSB oil close to breakup is fit by the elasto-capillary limit of the Oldroyd-B model (dash-dotted line). To quantitatively describe both regions, the full Oldroyd-B model with the additional solvent term (solid line) and IRT (dashed line) models are fit to the experimental observations. For the CSB oil in (b), the IRT model can extend the fitting validity up to $t \approx$ 100ms, but only the Oldroyd-B model can successfully predict the exponential region close to breakup. For the M1 oil shown in (c), both models yield good fits to the available data, but the Oldroyd-B model which includes an extra parameter produces a superfluous exponential decay at the end of breakup region. The values of the fit parameters are shown in Table 3.

for both oils. Notably, this value is smaller than the actual breakup times obtained from experiments for both oils. This discrepancy in the predicted and observed breakup time can be better visualized in Fig. 5(b) and (c) by switching the ordinate of $D(t)$ shown in (a) to a logarithmic scale. It is clear that the evolution in $D(t)$ for both oils progressively deviates from the Newtonian prediction for $t \gtrsim$ 90ms. This time range corresponds to Region 2 in Fig. 3, in which the shapes of the liquid bridges grow more slender and the strain rates grow progressively larger. The time-varying strain

rate in material elements at the minimum filament diameter can be defined as

$$\dot{\epsilon}_{mid}(t) = -\frac{2}{D(t)}\frac{dD(t)}{dt}. \tag{6}$$

It is clear from Fig. 5(b) that the evolution of $D(t)$ for the CSB oil exhibits an exponential decay with time close to breakup. This trend is reminiscent of the solution for the Oldroyd-B model in the limit of elasto-capillary thinning, which was first analyzed by Entov and Hinch [45]. The corresponding prediction for the filament diameter can be expressed as

$$D^{EC}(t) = \left(\frac{4GR_0}{\Gamma}\right)^{1/3}\exp\left(-\frac{t}{3\lambda}\right), \tag{7}$$

where G and λ are the elastic modulus and the relaxation time in the elasto-capillary thinning solution, respectively. By fitting Eq. (7) to the experimental data in Region 2 ($t > 90$ms) presented in Fig. 5(b) (shown as the dash-dotted line), we can extract a relaxation time of $\lambda = 4.56$ms. In this stage of thinning, the dimensionless strain rate, or the Weissenberg number defined as $Wi = \lambda\dot{\epsilon}_{mid}$ remains at a constant value of $Wi = 2/3$ [45]. Therefore, the retardation of breakup for both oils in Fig. 5(a) corresponds to a transition in the dominant force balance that governs capillary thinning dynamics as the filament diameter $D(t)$ decreases. For $t \lesssim 90$ms, the capillary thinning dynamics are governed by a visco-capillary (VC) balance. Because the viscosities and surface tensions of both oils are similar, the evolution of $D(t)$ for both oils overlaps and is consistent with the prediction for a viscous Newtonian fluid. As the filament thinning progresses beyond $t = 90$ms, the local strain rate $\dot{\epsilon}_{mid}$ near the pinch-off position increases. The dynamics of filament thinning for both oils become progressively dominated by elasto-capillary (EC) interactions, and the evolution of $D(t)$ with time is retarded, consistent with an apparent rate-thickening phenomenon in the instantaneous extensional viscosity $\eta(\dot{\epsilon})$ that would be extracted from a local application of Eq. (6). It is clear that the predictions of the viscous Newtonian fluid model and the elasto-capillary limit of Oldroyd-B model can be used in a piecewise manner to interpret the full capillary thinning dynamics of the CSB oil. However, it is desirable to develop a more comprehensive constitutive model incorporating both Newtonian and rate-dependent contributions to reconcile the non-Newtonian behavior of both oils in an extensional flow and to extract the relevant rheological parameters more systematically. We consider two possible model frameworks in the next section.

3.1. Oldroyd-B model

The full Oldroyd-B model is a well-studied constitutive equation used to characterize the rheology of common viscoelastic liquids such as Boger fluids and a number of dilute polymer solutions [18, 22, 46]. We have applied the elasto-capillary limit of this model (Eq. 7) to characterize the capillary thinning dynamics of the CSB oil close to breakup. However, to interpret the full range of the experimental data, we need to apply the complete form of the constitutive equation, which consists of a Newtonian solvent term and a viscoelastic term governed by the Upper-

Convected Maxwell (UCM) model [18]. Mathematically, the stress can be expressed as

$$\boldsymbol{\sigma} = \eta_S \boldsymbol{\gamma}_{(1)} + \boldsymbol{\sigma}_p, \tag{8a}$$

$$\boldsymbol{\sigma}_{p(1)} + \frac{1}{\lambda}\boldsymbol{\sigma}_p = G\boldsymbol{\gamma}_{(1)}. \tag{8b}$$

where η_S is the solvent viscosity, and $\boldsymbol{\sigma}_p$ is the viscoelastic stress. In Eq. (8b), G and λ are the relaxation time and elastic modulus in the UCM model. The subscript (1) denotes the first upper-convected derivative of the strain and stress tensors. Substituting Eq. (8) into the stress balance equation, Eq. (2), previous studies [25, 47] have found two asymptotic capillary thinning behaviors in the limits of low and high strain rates $\dot{\epsilon}$. When the Weissenberg number $Wi = \lambda\dot{\epsilon} \ll 2/3$, the stress arising from the Newtonian solvent dominates the capillary thinning dynamics. The evolution of $D(t)$ asymptotically approaches a linear decay, which is consistent with the prediction of Newtonian fluids under VC interaction (Eq. (5)). As $D(t)$ decreases progressively, the Weissenberg number increases and approaches $Wi = 2/3$. At this time, the non-Newtonian contribution to the overall normal stress difference $\Delta\sigma^{nN} = \sigma_{p,zz} - \sigma_{p,rr}$ exceeds the Newtonian stress arising from the solvent term $3\eta_S\dot{\epsilon}$ [47]. Thereafter, the resulting capillary thinning dynamics are asymptotically dominated by the balance of elasticity and capillarity (EC), and the evolution of $D(t)$ approaches the elasto-capillary limit as expressed in Eq. (7).

We numerically fit the elasto-capillary solution of the full Oldroyd-B model to the filament thinning data in Fig. 5(a), and the results are shown in Fig. 5(b) and (c) as solid lines. From Fig. 5(b), it is clear that this constitutive model successfully captures the evolution of $D(t)$ for the CSB oil over the time range of 40ms$\leq t \leq$ 120ms, in which the capillary thinning dynamics are controlled first by a visco-capillary (VC) balance and eventually an elasto-capillary (EC) balance. For the M1 oil, while the Oldroyd-B model leads to a good fit to the experimental data, it continues to predict exponential decay with time close to breakup, as shown in Fig. 5(c). This trend is not evident in the measurements over the range of data that can be resolved experimentally. Therefore, the full Oldroyd-B model is prone to data overfitting with low confidence in the value of the relaxation time or the time to breakup predicted by the regression.

3.2. Inelastic Rate-Thickening (IRT) model

From Fig. 5(c), it is clear that the evolution of $D(t)$ for the M1 oil deviates from the prediction of Newtonian fluids close to breakup, but also does not exhibit a distinct elasto-capillary balance, as described by the Oldroyd-B model. Other non-linear constitutive models such as the FENE-P or Giesekus models [47, 48], while providing an analytic solution of the capillary thinning dynamics, also introduce additional parameters and again lead to an overfitting of the available experimental data. A simpler model with a minimal set of constitutive parameters is needed to capture the key rheological features of these weakly rate-thickening materials in both shear and extensional flows. Here, we

12

propose a simple Inelastic Rate-Thickening (IRT) model suitable for extensional or shear flow. Inspired by Debbaut and Crochet [49], this model is expressed in the form of a generalized Newtonian fluid (GNF) [18, 50] as

$$\boldsymbol{\sigma} = \eta(\text{II}_{\dot{\gamma}}, \text{III}_{\dot{\gamma}})\dot{\boldsymbol{\gamma}}. \tag{9}$$

Here, to ensure frame invariance and to capture the difference between shear and extensional flows, the scalar viscosity η is written as a function of both the second and third invariants of the strain-rate tensor. The two invariants are defined [18] as

$$\text{II}_{\dot{\gamma}} = \text{tr}\,(\dot{\boldsymbol{\gamma}} \cdot \dot{\boldsymbol{\gamma}}), \tag{10a}$$

$$\text{III}_{\dot{\gamma}} = \text{tr}\,(\dot{\boldsymbol{\gamma}} \cdot \dot{\boldsymbol{\gamma}} \cdot \dot{\boldsymbol{\gamma}}). \tag{10b}$$

From Eqn. (10), Debbaut and Crochet [49] define the characteristic shear and extensional rates, $\dot{\gamma}$ and $\dot{\epsilon}$ in a general form as

$$\dot{\gamma}(\text{II}_{\dot{\gamma}}, \text{III}_{\dot{\gamma}}) = \sqrt{\frac{1}{2}\text{II}_{\dot{\gamma}}}, \tag{11a}$$

$$\dot{\epsilon}(\text{II}_{\dot{\gamma}}, \text{III}_{\dot{\gamma}}) = \frac{\text{III}_{\dot{\gamma}}}{\text{II}_{\dot{\gamma}}}. \tag{11b}$$

Notice that these definitions are consistent with Eq. (1) for homogeneous simple shear or extensional flows. For the weakly rate-thickening M1 oil, because the deviation from Newtonian behavior only occurs in extensional flows at high strain rates, we consider the *simplest possible form* of the rate-dependent viscosity $\eta(\dot{\epsilon})$ written as a function of the extensional rate $\dot{\epsilon}$ and evolving according to

$$\eta(\text{II}_{\dot{\gamma}}, \text{III}_{\dot{\gamma}}) = \eta_0 + k_2\dot{\epsilon} = \eta_0 + k_2\frac{\text{III}_{\dot{\gamma}}}{\text{II}_{\dot{\gamma}}}, \tag{12}$$

where η_0 is the zero-shear viscosity, and k_2 is a second-order material coefficient characterizing the rate of extensional thickening. From Eq. (12), this two-parameter IRT model features the simplest possible (linear) rate-dependence of the extensional viscosity, and incorporates stress contributions from both the solvent and the dispersed polymer or additive phases. It is worth noting that this form of $\eta(\dot{\epsilon})$ in Eq. (12) can also be obtained from the Oldroyd-B model in the limit of $Wi = \lambda\dot{\epsilon} \ll 1$ [51], where the terminal extensional viscosity is reduced to a linear function of the extensional rate $\dot{\epsilon}$ as

$$\eta_E = 3\eta_S + \frac{2G\lambda}{1 - 2\lambda\dot{\epsilon}} + \frac{G\lambda}{1 + \lambda\dot{\epsilon}} \xrightarrow{\lambda\dot{\epsilon} \ll 1} 3(\eta_S + G\lambda) + 3G\lambda^2\dot{\epsilon}. \tag{13}$$

We further demonstrate in Appendix B that Eq. (12) is consistent with the second-order fluid model in the limit of a slow and slowly varying extensional flow [18, 25]. As a result, this IRT model provides a consistent description of the material response within the framework of well-studied constitutive models for capillary thinning over an intermediate strain-rate range. In this range, the Newtonian and non-Newtonian contributions to the overall stress are both comparable in magnitude and they jointly lead to weakly rate-thickening behavior in the capillary thinning dynamics.

By substituting Eqs. (9)- (12) into Eq. (2), the dynamics of the IRT model in the capillarity-driven thinning process can be computed numerically. The experimental data in the time range of $t > 40$ms are then fit with the solution of IRT model, as shown in Fig. 5(b) and (c) as dashed lines. For the M1 oil (Fig. 5(b)), the IRT model can fit the evolution of $D(t)$ until end of the data ($t \approx 105$ms). For the CSB oil (Fig. 5(c)), however, the best IRT fitting only agrees with the experimental data until $t \approx 100$ms, and a clear deviation is observed closer to breakup. Compared with the prediction of the Newtonian model (dotted lines), the IRT model leads to a better fit to the experimental data because of the additional rate-dependent term in Eq. (12). However, as the evolution of the filament diameter $D(t)$ progresses, the corresponding strain rate $\dot{\epsilon}_{mid}(t)$ increases according to Eq. (6). The material response can thus have higher-order dependence on the strain rate, which lead to a stronger retardation in the approach to breakup beyond the prediction of the IRT model. This is shown for the CSB oil in the region of $t \gtrsim 100$ms in Fig. 5(c). The exponential thinning close to breakup indicates a sharper transition from VC to EC thinning, which can be better described by the Oldroyd-B model. By contrast, the 2-parameter IRT model with a first-order dependence of the extensional viscosity on strain rate cannot characterize such a substantial transition in the capillary thinning dynamics.

Table 3 lists the values of the fit parameters obtained from different constitutive models for both oils. Although the IRT model cannot capture the final capillary thinning of the CSB oil very close to breakup, the zero-shear viscosity is still consistent with the results from Newtonian and the elasto-capillary limit of Oldroyd-B model. Notice that the values of zero-shear viscosities, η_0 for the IRT model and $\eta_0 = \eta_S + G\lambda$ (from Eq. (13)) for the Oldroyd-B model are "apparent values", and are expected to be 2.35 times the viscosity obtained from shear viscosity measurements. This discrepancy originates from the different assumptions incorporated in the analysis of liquid bridge profiles during the thinning process. In the Newtonian analysis, the filament is assumed to develop a slender self-similar profile $R(z, t)$ dominated everywhere by a visco-capillary balance, whereas in the other two models perfectly cylindrical shapes are assumed with R independent of the axial position z. As a result, different geometric correction factors X must be applied in Eq. (2) to obtain quantitative values of the viscosity rather than only the correct scaling [30]. The apparent viscosity η_{app} and true viscosity η are connected through

$$\eta_{app} = \frac{2X - 1}{2X^N - 1}\eta,$$

(14)

where $X = 1$ is the geometric correction factor for the perfectly cylindrical filaments analyzed using the IRT model or

the Oldroyd-B model, and $X^N = 0.7127$ is the appropriate value of this coefficient for the self-similar visco-capillary balance of a Newtonian fluid [29, 30]. From Table 3, the numerical values of the material parameters generally show consistency among the different models at low strain rates. This demonstrates that the IRT model is able to correctly capture the observed capillary thinning dynamics when the material is weakly rate-thickening.

Table 3: Model parameters of different constitutive models for the two motor oils extracted from fitting their capillary thinning dynamics. Four models are tested: Newtonian, elasto-capillary limit of Oldroyd-B (only for the CSB oil), Oldroyd-B and IRT models. The parameters of Newtonian and the elasto-capillary limit of Oldroyd-B models are obtained by directly fitting Eq. (5) and Eq. (7). The constitutive parameters of the Oldroyd-B and IRT models are obtained by numerical solution of the evolution equations for filament diameter and stress in MATLAB. The differences among the Newtonian viscosity η_0, zero-rate viscosity $(\eta_S + G\lambda)$ in the Oldroyd-B model, and η_0 in the IRT model originate from the different slenderness assumptions of the liquid bridge profiles.

Model	No. of parameters	Parameters	CSB	M1
Newtonian	1	$\eta_0[\text{Pa} \cdot \text{s}]$	0.138	0.141
Oldroyd-B (EC limit)	2	$\lambda[\text{ms}]$	4.56	N/A
Oldroyd-B	3	$\eta_S[\text{Pa} \cdot \text{s}]$ $G[\text{Pa}]$ $\lambda[\text{ms}]$	0.236 9.49 4.94	0.254 23.44 2.44
IRT	2	$\eta_0[\text{Pa} \cdot \text{s}]$ $k_2[\text{Pa} \cdot \text{s}^2]$	0.215 1.14×10^{-3}	0.290 6.47×10^{-4}

3.3. Flow curves extracted from extensional rheometry

As shown in Fig. 5, the retardation of breakup observed with both motor oils corresponds to a weak extensional-rate-thickening phenomenon. To visualize this, we extract the strain rate $\dot{\epsilon}_{mid}(t)$ (from Eq. (6)) and the apparent extensional viscosity $\eta_{app}(t)$ from the temporal evolution of the filament diameter $D(t)$. In practice, the first-order derivative $\dot{D}(t)$ is obtained using a Savitzky-Golay filter with a polynomial order n and a filtering length $2L + 1$ [52]. Here, the set of parameters is applied according to a previous study [53]: $n = 2$ and $L = 14$. The original and smoothed data are carefully compared, and only the data points differing by less than 1% are retained for fitting. The apparent extensional viscosity can be defined as

$$\eta_{E,app} = \frac{2\Gamma/D(t)}{\dot{\epsilon}_{mid}(t)} = -\frac{\Gamma}{\dot{D}(t)}, \tag{15}$$

where Γ is the surface tension. The expression in Eq. (15) relies solely on experimental data and thus acts as an effective measure of the instantaneous extensional viscosity in the thinning process independent of the model choice. Similar to Eq. (14), the true extensional viscosity η_E can be recovered using the model-specified geometric correction factor X through a relationship of the form $\eta_E = (2X - 1)\eta_{E,app}$.

We compare the curve of apparent extensional viscosity against the extensional rate $\eta_{E,app}(\dot{\epsilon}_{mid})$ computed from the measured thinning profile with the predictions from the four constitutive models using the fit parameters from Table 3. The final results are plotted in Fig. 6(a) and (b). In these figures, the self-similar visco-capillary solution for a Newtonian fluid of viscosity η_0 predicts an apparent extensional viscosity $\eta_{E,app} = 3\eta_0/(2X^N - 1) = 7.05\eta_0$

15

215 (dotted line). In the elasto-capillary limit of the Oldroyd-B model (dash-dotted line), the apparent extensional viscosity diverges at a critical strain rate of $\dot{\epsilon}_c = 2/(3\lambda)$. The apparent extensional viscosity in the Oldroyd-B model (solid line) $\eta_{E,app}$ is solved numerically using Eq. (2) and (8), while the IRT model (dashed line) gives an analytical expression of $\eta_{E,app} = 3\eta_0 + 3k_2\dot{\epsilon}$.
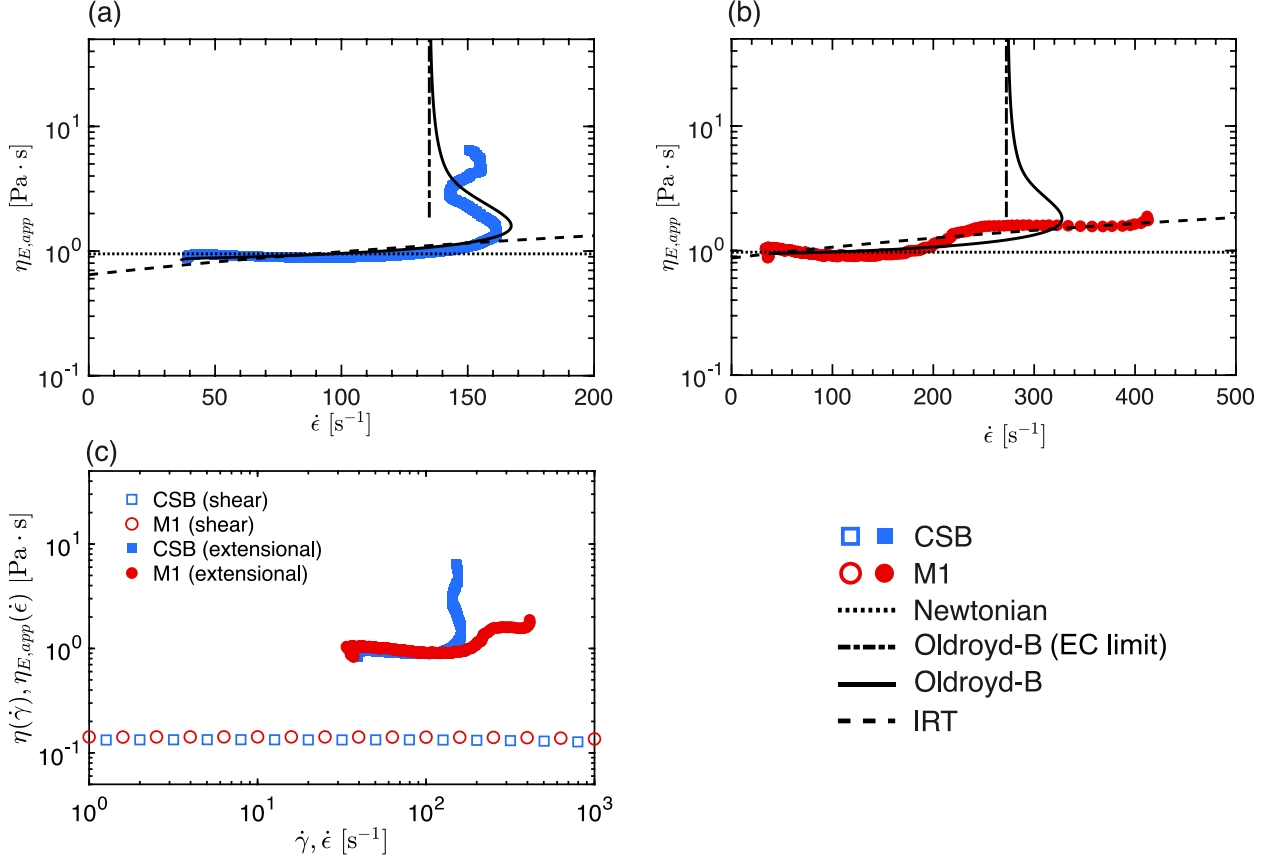

Figure 6: Apparent extensional viscosity $\eta_{E,app}$ against strain rate $\dot{\epsilon} = \dot{\epsilon}_{mid}$ for the two motor oils: (a) CSB. (b) M1. The experimental strain rates $\dot{\epsilon}_{mid}$ are extracted using a Savitzky-Golay filter ($n = 2$ and $L = 14$), and the apparent extensional viscosity can be calculated according to $\eta_{E,app} = 2\Gamma/(D(t)\dot{\epsilon}_{mid}(t))$. For both fluids, the apparent extensional viscosity $\eta_{E,app}$ is approximately constant at low strain rates $\dot{\epsilon}$, and it increases progressively as $\dot{\epsilon}$ increases, showing a weakly rate-thickening effect. The predictions from different constitutive models are plotted in the figures, including the Newtonian model (dotted line), elasto-capillary (EC) limit of the Oldroyd-B model (dash-dotted line), the Oldroyd-B model (solid line) and the IRT model (dashed line). (c) The apparent extensional viscosity $\eta_{E,app}(\dot{\epsilon})$ is contrasted with the shear viscosities $\eta(\dot{\gamma})$ obtained from a commercial shear rheometer. The rate-thickening is exclusively observed in extensional flow and varies substantially between the two fluids, even though they exhibit identical shear viscosities.

As we show in Fig. 6(a) and (b), the apparent extensional viscosities $\eta_{E,app}$ of both motor oils have a complex rate 220 dependence. For the CSB oil (Fig. 6(a)), at a low strain rate $\dot{\epsilon}_{mid} \lesssim 150\text{s}^{-1}$, $\eta_{E,app}$ remains approximately constant. This agrees with the prediction from the Newtonian model (dotted line), demonstrating that the capillary thinning dynamics are initially governed by a visco-capillary balance. Predictions from the Oldroyd-B and IRT models also compare well with the experimental data in this strain-rate range. However, as the strain rate further increases, $\eta_{E,app}$

16

rapidly increases and diverges at $\dot{\epsilon}_{mid} \approx 150\text{s}^{-1}$. This rapid increase of $\eta_{E,app}$ suggests a strongly viscoelastic response

that can be asymptotically described by the elasto-capillary limit of the Oldroyd-B model when $\lambda\dot{\epsilon}_{mid} \rightarrow 2/3$. By retaining both the Newtonian (solvent) and viscoelastic terms, the numerical solution to the full Oldroyd-B model can characterize the evolution in the experimental data at both low and high strain rates. For the M1 oil (Fig. 6(b)), the experimental data at low strain rates again agree with the predictions from the Newtonian, Oldroyd-B and IRT models. However, the apparent extensional viscosity $\eta_{E,app}$ for the M1 oil increases much less rapidly with strain rate than

the CSB oil, and an elasto-capillary balance, which corresponds to an exponential thinning at a constant strain rate is never attained, instead the strain rate continues to grow. This gradual increase is well captured by the IRT model, and shows is distinctly different from the prediction of the Oldroyd-B model.

To quantify the rate-thickening phenomena that can be measured with this customized CaBER system, we compare the measured apparent extensional viscosity for these two motor oils with the shear rheology data obtained from a

commercial shear rheometer (DHR-3, TA Instruments) using a 60mm, 2° cone-and-plate geometry. The results are plotted respectively against the shear and extensional rates, $\dot{\gamma}$ and $\dot{\epsilon}$ as defined in Eq. (11). As shown in Fig. 6(c), rate-thickening phenomena are observed for each motor oil only in extensional flow beyond a strain rate of approximately $150s^{-1}$. The apparent extensional viscosity can increase by as much as one order of magnitude at high strain rates.

As shown in Fig. 5 and 6, the Oldroyd-B and IRT models can successfully capture the extensional rheology of

the two motor oils and their distinct nonlinear viscoelastic features, which cannot be effectively detected from shear rheometry. Even at low concentrations, the presence of particulate and polymeric additives systematically modify the extensional rheology of those synthetic motor oil blends especially at high strain rates. In Appendix C and D, we use gel permeation chromatography (GPC) and PTFE filters to characterize the high-molecular-weight components in the two motor oils. A set of control experiments show that these low-concentration macromolecular additives

can significantly alter the extensional rheology of the two products. The rate-thickening response observed using our customized CaBER system demonstrates that these types of motor oils are not ideal Newtonian fluids as previous studies have indicated, and the range of strain rates where we observe rate-thickening phenomena are closely connected to important industrial processes including jetting, coating and stamping [54].

3.4. Choice of constitutive model

Unlike filament-stretching rheometry [51] in which an extensional rate is imposed externally, the CaBER technique

relies on analysis of the capillarity-driven thinning dynamics to extract extensional rheological properties. Therefore, successful rheological characterization relies on choosing the best-fit constitutive model with physically interpretable parameters to describe the data. From Fig. 6, we see that the best-fit model must capture the evolution in rheological characteristics with strain rate, with a minimal number of model parameters to avoid overfitting. In Sec. 3.3, we

used insight and experience to select different constitutive models that can characterize the distinct capillary thinning

dynamics of the two motor oils. In industrial applications, however, a more autonomous process is desirable: can we select the best-fit constitutive model from regression to CaBER measurements? This process requires an intimate understanding of the capillary thinning dynamics for different constitutive models. With the help of robust imaging techniques, this process can potentially be automated to provide a rapid testing protocol to recognize and quantify the extensional rheology of an unknown fluid.

In Fig. 7(a), we sketch the evolution of the mid-plane radius $R_{mid}(t)$ using the capillary thinning process for a number of well-studied constitutive models. In Fig. 7(b) and (c), the corresponding evolution of strain rate $\dot{\epsilon}(t)$ and apparent extensional viscosity $\eta_{E,app}(\dot{\epsilon})$ are also plotted. On the basis of these distinct profiles, capillary thinning dynamics can be divided into four categories: (a) rate-thinning inelastic models, such as the Bingham plastic and power-law fluid; (b) the rate-independent (Newtonian) model; (c) weakly rate-thickening models, such as the IRT model introduced in Eq. (9); (d) strongly viscoelastic models, such as Oldroyd-B and FENE-P fluids. In Table 7, the evolutions of $R_{mid}(t)$ and $\eta_{E,app}$ for each model are explicitly expressed and compared.

Table 4: List of common constitutive models and the corresponding expressions for the evolution in mid-plane radius $R_{mid}(t)$ and apparent extensional viscosity $\eta_{E,app}$, as well as whether the results are obtained analytically.

Model	$R_{mid}(t) =$	$\eta_{E,app} =$	Analytical?	Ref.
Bingham plastic	$\dfrac{\Gamma}{\sqrt{3}\tau_y}\left\{1 - \exp\left[\dfrac{\tau_y(t - t_C)}{2\sqrt{3}\eta_0}\right]\right\}$	$3\eta_0\exp\left[\dfrac{\tau_y(t_C - t)}{2\sqrt{3}\eta_0}\right]$	Yes	[25]
Power law fluid	$R_0\Phi(n)\dfrac{\Gamma}{K}(t_C - t)^n$	$\dfrac{K}{2R_0\Phi(n)\Gamma n(t_C - t)^{n-1}}$	Numerically	[25, 55]
Newtonian fluid	$0.0709\dfrac{\Gamma}{\eta_0}(t_C - t)$	$\dfrac{3}{2X^N - 1}\eta_0 = 7.05\eta_0$	Yes	[29, 30, 32]
IRT	$Wi \ll 1:\ \dfrac{1}{6}\dfrac{\Gamma}{\eta_0}(t_C - t)$ $Wi \sim O(1):\ \dfrac{\Gamma}{48k_2}(t_C - t)^2$	$3\eta_0 + 3k_2\dot{\epsilon}$	Yes	This work
Oldroyd-B (EC limit)	$\left(\dfrac{GR_0^4}{2\Gamma}\right)^{1/3}\exp\left(-\dfrac{t}{3\lambda}\right)$	Diverging	Yes	[45]
Oldroyd-B	Numerically solved	$Wi \ll 2/3:\ 3\eta_S$ $Wi \to 2/3:$ Diverging	Numerically	[46, 56]
FENE-P	Numerically solved	Early time: $3\eta_S$ $Wi \sim 2/3:$ rapidly growing $Wi \gg 2/3:\ \eta_{E,\infty} = 2G\lambda L^2$	Numerically	[45, 25]

The capillary thinning dynamics of a Newtonian fluid (black line shown in Fig. 7) have been extensively studied
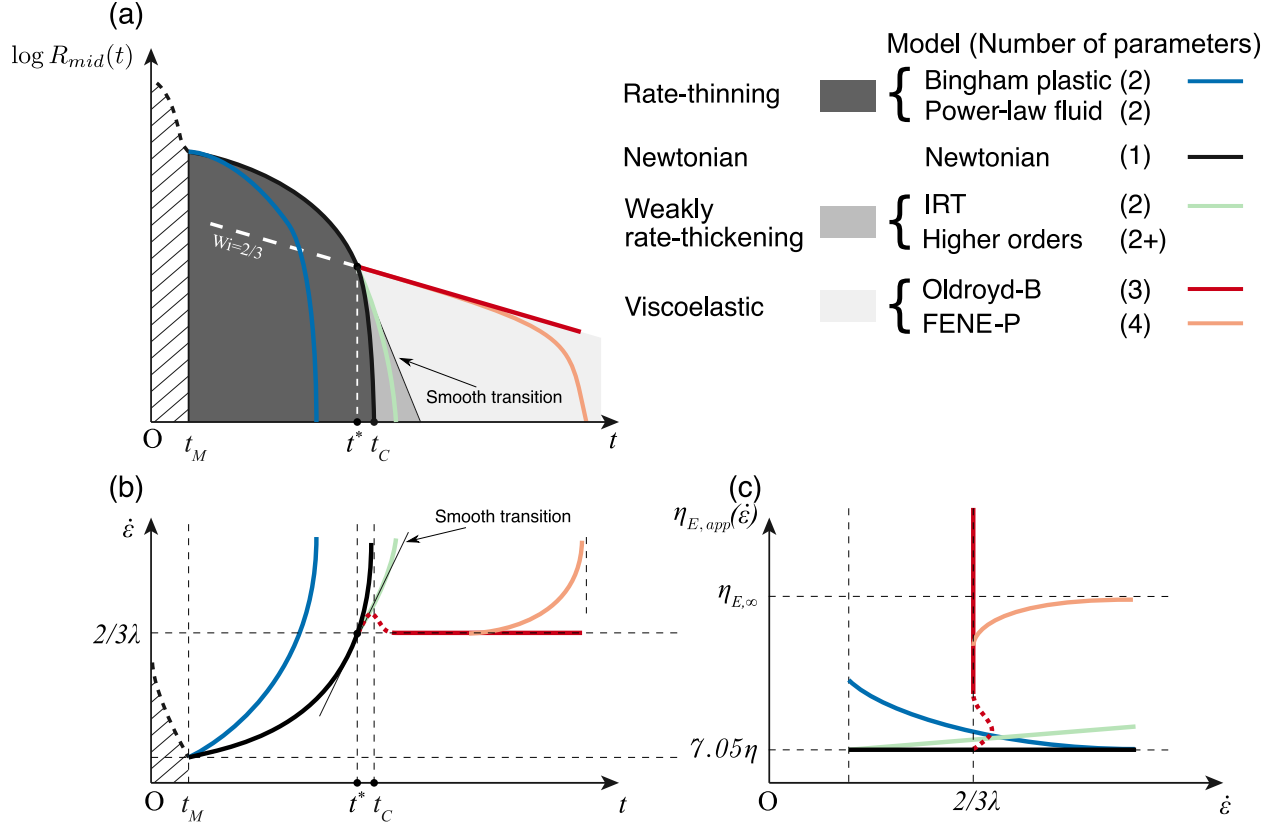
Figure 7: Schematic of capillary thinning dynamics for different common constitutive models, categorized into rate-thinning models (e.g. Bingham plastic ━━), Newtonian model (━━), weakly rate-thickening models (IRT ━━) and viscoelastic models (Oldroyd-B ━━, FENE-P ━━). The hatched region indicates the initial step time when the discs are in motion until t_M. In a strongly viscoelastic fluid at time t^*, the initial VC thinning transitions to an EC balance as illustrated by the Oldroyd-B model. (a) Temporal evolution in the mid-plane radius, $\log R_{mid}(t)$. At a critical time t_C, filament breakup is predicted by the Newtonian model. Different shaded-gray regions indicate distinct categories of materials based on their capillary thinning dynamics, as shown in the legend. The thin solid line indicates the tangent line to the evolution of mid-plane radius for the Newtonian model at $t = t^*$. (b) Temporal evolution in the strain rate $\dot{\epsilon}(t)$. The relaxation time in the Oldroyd-B model is given by λ. (c) Evolution in $\eta_{E,app}$ with the instantaneous strain rate $\dot{\epsilon}$. The terminal apparent extensional viscosity at finite extensibility in the FENE-P model is given by $\eta_{E,\infty} = 2G\lambda L^2$. The number of constitutive parameters in each model is noted in the brackets in the legend.

both analytically and experimentally [29, 30, 32]. When a visco-capillary balance is established, the mid-plane radius $R_{mid}(t)$ decays linearly with time as indicated in Fig. 5(a). This is the simplest constitutive response and is described by only one model parameter, the Newtonian viscosity η_0, and this gives rise to a constant true extensional viscosity $\eta_E = 3\eta_0$, or equivalently, an apparent extensional viscosity of $\eta_{E,app} = 7.05\eta_0$ as shown in Fig. 7(c) as a result of the nontrivial axial filament curvature. The strain rate $\dot{\epsilon}$ diverges as $\dot{\epsilon} \sim 2/(t_C - t)$ close to the finite breakup time $t_C = \eta_0 R_0/(0.0709\Gamma)$, where R_0 is the initial filament radius. The evolution of $R_{mid}(t)$ for a rate-thinning Generalized Newtonian fluid model (blue line) is *always* located below the prediction of the Newtonian model within the dark gray region, and $\ddot{R}_{mid}(t) < 0$ at all time. While this condition might not be easy to distinguish in a semilogarithmic plot of $R_{mid}(t)$, rate-thinning models can be clearly distinguished from other models by a decreasing apparent extensional

viscosity $\eta_{E,app}(\dot{\epsilon})$, as shown in Fig. 7(c). Common inelastic constitutive models for rate-thinning materials include the Bingham plastic, power-law fluid, and Herschel-Bulkley fluid models [25, 33]. These models contain two or more constitutive parameters to fully characterize the zero-rate viscosity and the degree of rate-thinning. The capillary thinning dynamics of dilute polymer solutions in a Newtonian solvent initially evolve close to the response expected for a Newtonian fluid, when a visco-capillary (VC) balance dominates the evolution of $R_{mid}(t)$, and the tensile stress difference in the filament is close to $\Delta\sigma \sim 3\eta_S\dot{\epsilon}(t)$, where η_S is the solvent viscosity. At a transition time t^*, however, $R_{mid}(t)$ begins to deviate systematically from the linear thinning response. For strongly extension-thickening materials described by bead-spring models, there is a sharp change in $\dot{R}_{mid}$ at t^* as indicated in Fig. 7(a), (see also Wagner et al. [47]). This transition has been documented by many recent experimental studies [57, 58]. The transition time t^* can be calculated by equating

$$R_{mid}^N(t^*) = R_{mid}^{EC}(t^*), \tag{16}$$

where $R_{mid}^N(t)$ and $R_{mid}^{EC}(t)$ are the solutions of the filament radius for the Newtonian model and the elasto-capillary limit of the Oldroyd-B model, as expressed in Eq. (5) and (7), respectively. The rapid decrease in $\dot{R}_{mid}$ and the exponential increase in the extensional stress difference also result in an overshoot in the strain rate $\dot{\epsilon}$ close to t^*, as shown by the red dashed line in Fig. 7(b). Such an overshoot can be physically explained by the non-monotonic temporal evolution of the rr-component in the stress tensor as an elastocapillary balance is established in the filament [47]. In the limit of infinite extensibility, the FENE-P dumbbell model becomes equivalent to the Oldroyd-B model and the apparent extensional viscosity $\eta_{E,app}$ diverges when the strain rate $\dot{\epsilon} \rightarrow 2/(3\lambda)$, or equivalently the Weissenberg number approaches $Wi = 2/3$. For the FENE-P model, the capillary thinning dynamics have also been extensively studied over the past few decades [45, 22, 47]. The evolution of mid-plane radius $R_{mid}(t)$ deviates from the exponential decay obtained by an elasto-capillary balance close to breakup as the polymer chains are stretched to their finite extensibility limit L. At this time, the microstructure of the fluid becomes highly anisotropic, and the capillary thinning dynamics again approach Newtonian-like behavior with a new terminal apparent extensional viscosity $\eta_{E,\infty} = 2G\lambda L^2$ [59].

Motivated by the results from the two motor oils in Figure 5, we identify an important intermediate weakly elastic capillary thinning regime, in which the evolution of the filament radius cannot be adequately described by either a Newtonian fluid or a viscoelastic bead-spring model. The two-parameter IRT model proposed in this paper (Eq. (9)) can capture this response by incorporating both a linear (Newtonian) viscous response and a second-order stress term. As shown in Fig. 7(a), the evolution of the filament radius falls into an intermediate regime shown by the light gray-shaded area close to breakup. Here, the capillary thinning is slightly retarded compared with a Newtonian fluid with the same zero-shear viscosity. However, no distinct transition between a VC and EC balance is expected, because both the linear ($3\eta_0\dot{\epsilon}$) and second-order ($3k_2\dot{\epsilon}^2$) contributions to the tensile stress difference remain comparable in magnitude throughout the capillary thinning process.

20

To clearly distinguish a weakly rate-thickening material (e.g. the IRT response) from a more strongly viscoelastic material (e.g. the Oldroyd-B or FENE dumbbell response), we use an elasto-capillary number $Ec = t_{EC}/t_{VC}^*$ to evaluate the magnitudes of the EC and VC interactions for different constitutive models. Here, $t_{VC}^* = \eta_S R_{mid}(t^*)/\Gamma$ is the visco-capillary timescale, evaluated using the filament radius at the crossover time t^* as the characteristic length scale. The characteristic elasto-capillary timescale t_{EC} is specific to each constitutive model and can be obtained from dimensional analysis: for the IRT model $t_{EC} = k_2/\eta_0$, and for the Oldroyd-B model $t_{EC} = \lambda$. Satisfying the constraint given by Eq. 16 is a necessary but not sufficient condition to determine the crossover time because both $R_{mid}(t^*)$ and t^* are unknown. However, a critical value for the elasto-capillary number (which we denote by Ec_c) separating strongly and weakly elastic fluids can be computed pragmatically by also matching the rates of thinning in the filament at the transition time $t = t^*$ obtained from Eq. (16) using the asymptotic solutions in Table 4, i.e. we also require

$$\dot{R}_{mid}^N(t^*) = \dot{R}_{mid}^{EC}(t^*) \tag{17}$$

as indicated by the black tangent line in Fig. 7. When both Eqs. 16 and 17 are satisfied, the two asymptotic solutions are C^1 continuous at $t = t^*$, and the critical elasto-capillary number can be calculated after some algebra to be

$$Ec_c \triangleq \frac{\lambda\Gamma}{\eta_S R(t^*)} = \frac{1}{3(0.0709)} \approx 4.7. \tag{18}$$

The critical filament radius $R(t^*)$ appearing in Eq. 18 can be determined directly from experiments as the point at which the evolution of the filament radius deviates from the prediction for the Newtonian fluid. If an *a priori* estimate of the elasto-capillary number is required, the critical filament radius $R(t^*)$ can also be replaced by the initial filament diameter R_0 to yield a conservative estimate of the elasto-capillary number without compromising the validity of this dimensionless criterion.

In summary, when $Ec < Ec_c$, the temporal evolution of $\log R(t)$ will be inflection-free, and from inspection of Fig. 7, this represents a weakly rate-thickening behavior. Fitting an exponential decay to the evolution of the filament profile is likely to result in overfitting and poor confidence in the resulting value of the extensional relaxation time. Using the results in Table 3, the elasto-capillary numbers for the CSB and M1 oils are approximately $Ec = 11.4$ and $Ec = 3.7$, respectively. We can thus justify that the Oldroyd-B model is likely to be a better-fit model for the CSB oil, which exhibits capillarity-driven thinning behavior dominated by an elasto-capillary balance close to breakup. In contrast, the M1 oil is evidently only a weakly rate-thickening material since $Ec \lesssim Ec_c$, and the IRT model better reflects the physical nature of the capillary thinning dynamics for this type of fluid. The dimensionless criterion embodied by Eq. 18 can be retroactively applied to a number of previously studied viscoelastic fluid systems [53, 57, 60], and we find this criterion to be completely consistent with the observed capillary thinning dynamics and

the respective authors' conclusions regarding the degree of extensional rate-thickening observed for a wide range of molecular weights and concentrations.

4. Conclusions

In this paper, the capillary thinning dynamics of two commercially available motor oils have been probed with a customized Capillary Breakup Extensional Rheometer (CaBER), from which their extensional rheological behaviors are extracted. Independent measurements of their shear rheology suggest that both fluids initially appear to be Newtonian. However, both fluids exhibit rate-thickening behaviors in extensional flow, resulting in retardation of the capillary thinning dynamics and a delayed time to breakup. As the strain rate increases, an elasto-capillary (EC) force balance progressively replaces the visco-capillary (VC) balance in controlling the capillary thinning dynamics. To model their unique rheological behavior in both shear and extensional flows, we considered a number of different constitutive models, including the Newtonian fluid and Oldroyd-B model (in the elasto-capillary limit or the full numerically computed solution). While a sufficiently elastic fluid sample can be described by the bead-spring models that have already been extensively studied, in the literature, such models poorly describe the capillary thinning dynamics of a more weakly rate-thickening sample. We thus propose a two-parameter Inelastic Rate-Thickening (IRT) model, which incorporates the zero-rate viscosity as well as the rate of extensional thickening. Compared with the Oldroyd-B model, this new IRT model leads to a more robust fit to the capillary thinning dynamics of the weakly rate-thickening sample.

We also have outlined a process to determine the best-fitting constitutive model from the observed capillary thinning dynamics of an unknown material. In particular, the choice of selecting a weakly rate-thickening, or more strongly strain-hardening, model depends not only on the quality of the image data and the accuracy of fitting, but also on the consistency of rheological features displayed by the model predictions and the experimental data. To automate this model selection process for faster rheological characterization, we carefully compared the capillary thinning dynamics of an inelastic Newtonian model and the elasto-capillary limit of the Oldroyd-B model. By balancing the rate of capillary thinning predicted by the models we arrived at a natural dimensionless constraint equivalent to a critical value of the elasto-capillary number Ec. When $Ec \lesssim 4.7$, a weakly elastic material response of the kind predicted by our two-parameter inelastic rate-thickening (IRT) framework is expected to provide the most parsimonious and reliable description of the data. Only when $Ec \gtrsim 4.7$ is a clear elasto-capillary thinning regime with a distinct exponential decay in filament radius (as described by Eq. 7) expected to be discernible. Comparing the model predictions and the values of Ec for the two motor oils considered in the present study, it becomes clear that the Oldroyd-B model is most appropriate for the CSB oil ($Ec = 8.6$), which exhibits the well-known exponential thinning behavior close to breakup. However, the M1 oil ($Ec = 4.2$) exhibits a more weakly elastic response, and the extensional rheology of this fluid is

better described by our inelastic rate-thickening (IRT) framework.

The two motor oils tested in this study are representative of a number of material systems featuring increased rheological complexity that originates from low-concentrated additives. Examples include colloid/particle suspensions and weakly elastic polymer solutions with Newtonian solvents. Due to the low solute concentrations, it can be difficult for shear rheometry to fully resolve the weak viscoelasticity of such fluids. However, these additives can substantially modify the rheology of the materials under more extreme working conditions featuring extensional kinematics. Rheological characterizations of these motor oils under high deformation rates using a customized CaBER system provide additional insight for more detailed and effective rheological characterizations. Furthermore, by combining CaBER data with more advanced image processing and data analysis techniques, plus an appropriate dimensionless criterion based on the elasto-capillary number (Eq. 18), this framework can be automated to yield a high-throughput screening process. We hope this work can help facilitate a better understanding of the extensional rheology for a wide range of poorly characterized complex fluids and blends, and subsequently support optimization of multiple industrial processes.

Appendix A. Calibrations and preliminary tests for the components of the customized CaBER system

Appendix A.1. Axial position control

As Fig. A.1 shows, the linear actuator is calibrated using three different strokes of 2mm, 5mm and 8mm. The temporal evolution of the linear motion is recorded by a high-speed camera at a frame rate of 5900fps. With manually fine-tuned PID parameters, the linear actuator shows a repeatable maximum velocity $v_{max} \approx 0.2$m/s with well controlled linearity and minimal position overshoot (8.7%, 4.9% and 2.7%). Under this condition, an overall stroke of 10mm (5mm stroke from each motor) defines an approximate actuation time $t_M = 25$ms, which is 50% less than a commercial CaBER system [42]. Furthermore, this actuating time t_M can be compared with the Rayleigh timescale t_R defined as

$$t_R = \sqrt{\frac{\rho R_0^3}{\Gamma}}. \tag{A.1}$$

Within this timescale, inertio-capillary (IC) interactions dominate the capillary thinning dynamics [61]. As a result, the established analytic solutions describing VC or EC thinning do not apply and rheological parameters cannot be readily
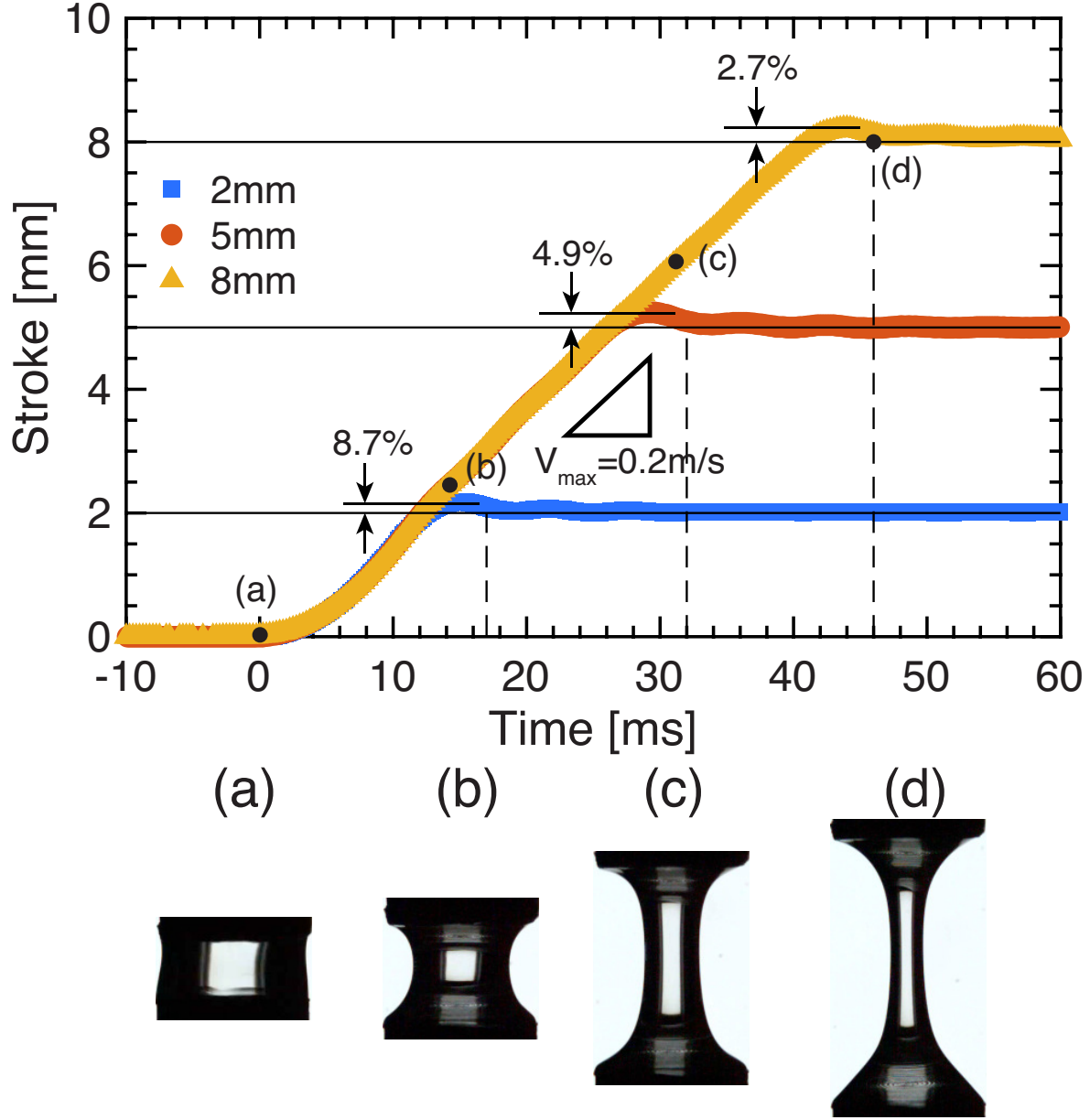
23

Figure A.1: Stroke tests for the linear actuator. The corresponding PID parameters are manually fine-tuned in the control software. Three stroke distances, 2mm, 5mm and 8mm are imposed with the highest possible actuating speed. The stroke trajectories are captured with a high-speed camera using a frame rate of 5900fps, from which the temporal evolution of the end discs is extracted. The measured displacements show good linearity with time in the rising region with a maximum velocity of 0.2m/s. The final settling times (vertical dashed lines) of the three strokes are approximately 17ms, 32ms and 46ms, with overshoots of 8.7%, 4.9% and 2.7%, respectively. The imposed strokes are illustrated in a real CaBER experimental setup as shown in (a)-(d) with the corresponding time stamps marked in the figure (·).

extracted. For common materials measured using the filament thinning technique such as water and low viscosity oils, Rayleigh timescales are in the range of $20 \lesssim t_R \lesssim 40$ms. Therefore, decreasing actuation time t_M allows measurement at earlier times and better distinction of VC and EC thinning.

Appendix A.2. Radial profile measurement

The laser micrometer is calibrated with a series of surface-finished aluminum rods and standard optical glass fibers with diameters measured by a caliper (precision: 5μm). As shown in Fig. A.2, the measured diameter and analog output voltage from the laser micrometer are plotted. In order to show the data on a logarithmic scale, all the measured voltages are offset by the ground voltage of $V_{min} = -5$V. Data in Fig. A.2 are fit with a linear ($R^2 = 0.990$) and third-order ($R^2 = 0.998$) polynomial. A second-order fit is not utilized here because of its monotonicity in the second-order derivative, which brings superfluous constraints to the data fitting. In general, the data show good linearity above the manufacturer-claimed minimum object size of 100μm (white region). Smaller objects down to 17μm can be imaged with the high-speed camera which is already configured for our customized CaBER system (yellow region). Below 17μm (pink region), measurements could also potentially be made with a macro lens of higher magnification.
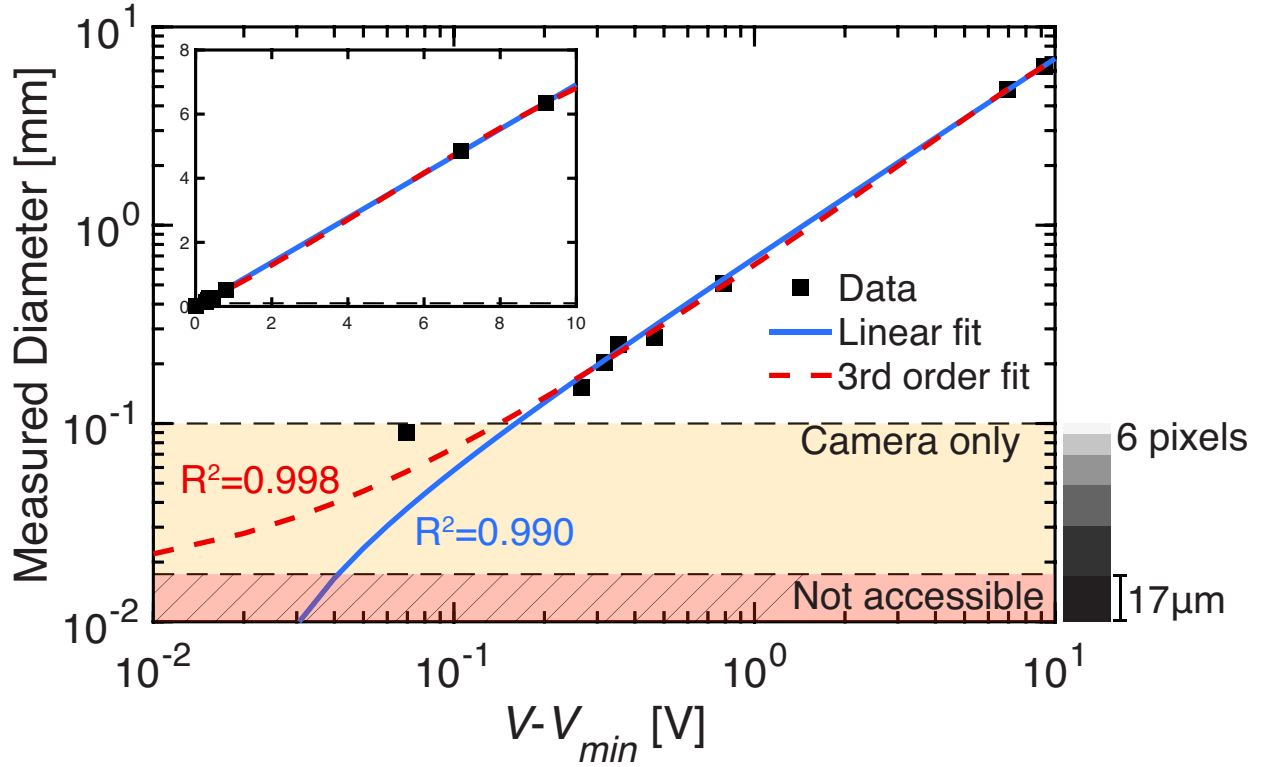

Figure A.2: Calibration of the laser micrometer. The laser micrometer is calibrated using a series of aluminum rods and optical fibers with independently measured diameters (with precision of 0.005mm). For each diameter, five consecutive measurements of the voltage outputs are performed and averaged. To plot on a logarithmic scale, the difference between measured voltage (V) and the ground voltage ($V_{min} = -5$V) is taken. Both linear and third-order polynomial fittings are performed to the data, and we obtain coefficients of determination of $R^2 = 0.990$ and $R^2 = 0.998$, respectively. The manufacturer claims a minimum object size of 100μm in diameter (white region), below which measurements can only be performed by a more delicate imaging system (yellow region). With the present optical system, we can reach an image resolution of 17μm/px (above pink region).

The beam thickness of the laser micrometer is measured to be approximately 100μm. This can be verified by

continuously feeding a flat linear motor head across the laser beam with a small step size of 5μm. As a result, the location of the mid-plane radius $R_{mid}(t)$ cannot be determined more precisely than this and can result in large errors when the axial radius of curvature of the filament is comparable with this thickness. Beyond this point, more accurate measurements can only be obtained from optical systems with higher resolution.

Appendix A.3. Temperature control

Temperature control of the customized CaBER system is demonstrated by performing measurements on a commercial butter (Kraft Food Group, Inc). Its viscosity is close to common automotive oils but can vary substantially over the temperature range of 30°C to 60°C. This feature makes it a good model fluid for illustrating the thermorheological changes in capillary thinning experiments. Within the chosen temperature range, measurements from a commercial shear rheometer (DHR-3, TA Instruments) shown in Fig. A.3(b) and (c) demonstrate that the shear viscosity is almost independent of shear rate but strongly dependent on temperature. The temperature-shear viscosity relation can be well-described by the Williams-Landel-Ferry (WLF) relation [62], which is expressed in Eq. (A.2) as

$$\frac{\eta(T)}{\eta(T_r)} = \exp\left[-\frac{C_1(T - T_r)}{C_2 + T - T_r}\right]. \tag{A.2}$$

By choosing a reference temperature $T_r = 30$°C close to the softening point we obtain the WLF parameters $C_1 = 3.47$ and $C_2 = 93.73$K. As shown in Fig. A.3(a), snapshots of the capillary thinning profiles of the butter can be captured in the customized CaBER system at different temperatures through the high-speed imaging system. As the temperature increases, the capillary thinning profiles that develop during the opening of the discs differ substantially, changing from a liquid bridge that forms between the end discs (at $T = 30$°C) to formation of satellite droplets (at $T = 60$°C). Using the material properties of the butter measured from shear rheometry, the Ohnesorge number $Oh = \eta_0/\sqrt{\rho\Gamma R_0}$ in the chosen temperature range evolves from 0.15 to 0.07. From the evolution of the capillary thinning profiles observed at different temperatures, we obtain a lower limit of $Oh_{min} \approx 0.15$, below which inertio-capillary interactions dominate the capillary thinning process, and the pinch-off of the liquid bridge is localized close to the liquid reservoir at one of the end discs. At Ohnesorge numbers $Oh < Oh_{min}$, the viscocapillary balance is not established and fluid constitutive parameters cannot be obtained. This lower limit is consistent with a previous study [42].

Appendix B. Rheological equivalence of the IRT and second-order fluid (SOF) models in the limit of a slow and slowly varying extensional flow

The retarded-motion expansion uses a polynomial expansion of the strain rate tensor $\dot{\gamma}$ as well as its upper-convected derivatives to construct the fluid constitutive equation [18]. Analogous to a Taylor-series expansion, the stress tensor σ in the retarded-motion expansion can be expressed as the addition of different-order upper-convected
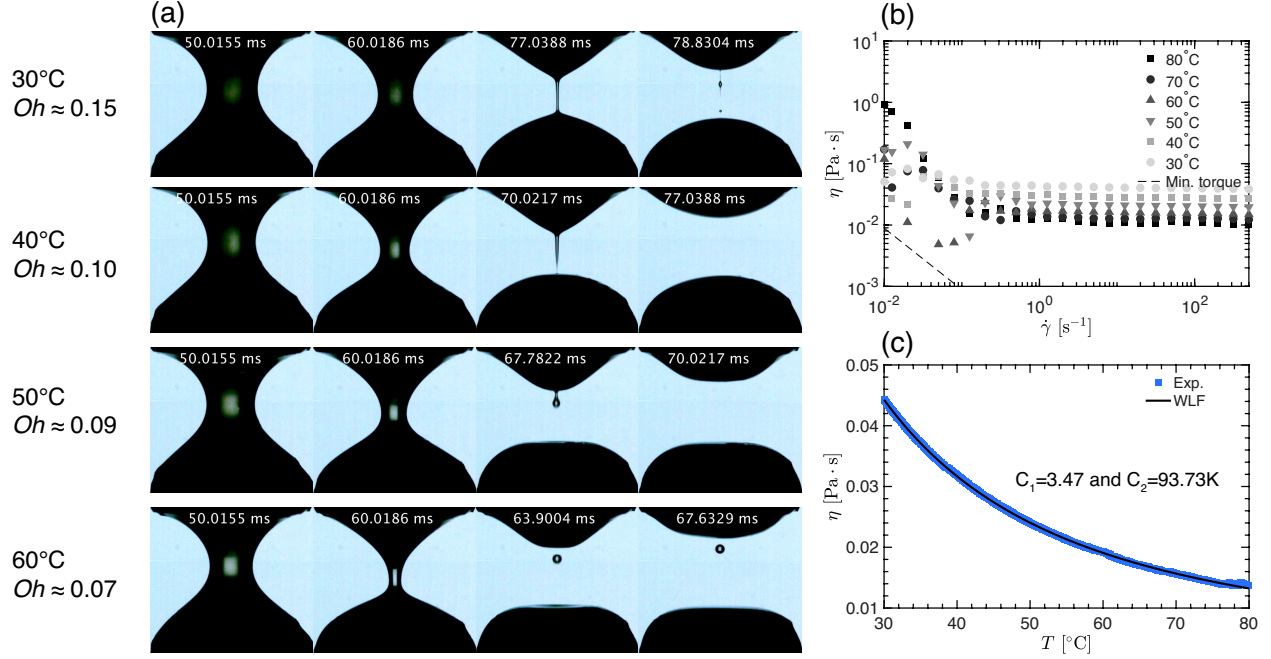
Figure A.3: Rheological tests on a commercial butter to demonstrate the temperature control on the customized CaBER system. (a) Snapshots of the capillary thinning profiles for the butter at different temperatures from 30°C to 60°C. The corresponding Ohnesorge number Oh ranges from 0.15 to 0.07. The disc diameter is $2R_0 = 6$mm, with initial and final gaps $L_0 = 2$mm and $L_f = 5.2$mm, leading to a Hencky strain $\epsilon = \ln L_f/L_0 \approx 0.96$. The snapshots show distinct viscosity-dependent thinning profiles at different temperatures: At 30°C, the VC thinning leads to a liquid bridge formed between the discs and a well-defined breakup time $t_C \approx 78$ms. As the Ohnesorge number Oh decreases with increasing temperature, the capillary thinning process becomes more localized, and inertio-capillary effects lead to droplet formation. A lower limit of $Oh_{min} \approx 0.15$ can be determined, above which valid rheological measurements through the filament thinning technique can be performed. (b) Shear viscosity of the butter against shear rate $\dot{\gamma}$ performed on a commercial shear rheometer. The results show Newtonian behavior within a shear-rate range of $10^{-2}\text{s}^{-1} \leq \dot{\gamma} \leq 500\text{s}^{-1}$. (c) Temperature ramp experiments of the butter performed on the commercial shear rheometer in a temperature range of $30°\text{C} \leq T \leq 80°\text{C}$. The experimental data are fit using the well-studied Williams-Landel-Ferry (WLF) equation, and we obtain the fit parameters $C_1 = 3.47$ and $C_2 = 93.73$K.

derivatives of $\dot{\gamma}$, which can be expressed as

$$\sigma = b_1\gamma_{(1)} + b_{11}\gamma_{(1)} \cdot \gamma_{(1)} + b_2\gamma_{(2)} + \ ......, \tag{B.1}$$

where the subscript indicates the n-th order upper-convected derivative and $\gamma_{(2)} = (\gamma_{(1)})_{(1)}$ [18]. The constants b_1, b_{11} and b_2 are the corresponding retarded-motion constants at each order. If only the first-order term is preserved, the retarded-motion expansion reduces to the Newtonian model with viscosity $b_1 = \eta_0$. By increasing the order of the expansion, the retarded-motion expansion can be used to describe slowly varying flows of fluid with increasing rheological complexity. In the principle of parsimony, however, a second-order fluid (SOF) model is commonly applied as the simplest form of a rate-dependent constitutive model. In the second-order fluid model, only the three terms in Eq. (B.1) are considered. In an extensional flow field under the condition of a slow and slowly varying flow,

27

which can be mathematically expressed as

$$Oh = \frac{b_1}{\sqrt{\rho \Gamma R_0}} \gtrsim O(1), \tag{B.2a}$$

$$\ddot{\epsilon} \ll \dot{\epsilon}^2, \tag{B.2b}$$

we can write the total normal stress difference from Eq. (B.1) as

$$\Delta \sigma^{nN} = \sigma_{zz} - \sigma_{rr} = 3b_1 \dot{\epsilon} + 3(b_{11} - b_2)\dot{\epsilon}^2 = \eta_E(\dot{\epsilon})\dot{\epsilon}. \tag{B.3}$$

The two independent parameters in this equation, b_1 and $(b_{11} - b_2)$ can be used to construct a characteristic strain rate $\dot{\epsilon}_c = b_1/(b_{11} - b_2)$, and thus an appropriate dimensionless measure of flow strength is the Weissenberg number $Wi = (b_{11} - b_2)\dot{\epsilon}/b_1$. Compared with Eq. (12), the second-order fluid model predicts a form of the extensional viscosity $\eta_E(\dot{\epsilon})$ that is consistent with the IRT model, in which $\eta_0 = b_1$, and $k_2 = b_{11} - b_2$. Given that $\Delta \sigma = 3\eta_S \dot{\epsilon} + \Delta \sigma^{nN}$, Eq. (B.3) can be readily substituted into Eq. (2) to calculate the evolution of $R_{mid}(t)$ during a capillarity-driven filament thinning process. McKinley [25] has identified two asymptotic solutions of the capillary thinning dynamics. When $Wi \ll 1$, the evolution of $R_{mid}(t)$ is reduced to the Newtonian solution with a linear decay in time. However, when Wi approaches unity, the mid-plane radius $R_{mid}(t)$ quadratically decreases with time $t_C - t$ close to breakup, where t_C is the breakup time of the filament, showing a progressive transition to a weakly rate-thickening response.

Appendix C. Gel permeation chromatography (GPC) of CSB and M1 oils

Gel permeation chromatography (GPC) is used to measure the molecular weight distribution of different components in both sample oils and to characterize their additive phases. This technique, introduced in 1964 by J.C. Moore [63], works by sieving components with different molecular sizes in the analytes by injecting a dilute solution into a gel column with precisely controlled pore sizes. The molecular size of these analytes, specified by the radius of gyration R_g determines the time a macromolecule takes to travel through the pores, defined as the retention time. Molecules with smaller sizes can be trapped deeper in the pores, and thus take longer to elute out. Finally, the corresponding molecular weights of separated species are measured with single or multiple detectors, such as reflective index (RI) detector, infrared (IF) or ultraviolet (UV) detectors, as well as a differential viscometer. Each of these detectors is sensitive to different molecular weight species. Using a calibration curve with known molecular weights, or by combining multiple different detectors, the molecular weight distribution of an unknown solute can thus be obtained.

In this paper, GPC experiments of both motor oils are performed with a reflective index (RI) detector. Tetrahydrofuran (THF) is chosen as the eluent at 30°C. The results are shown in Fig. C.1, where the relative number concentration RC is plotted against the molecular weight M. Monodisperse polystyrenes dissolved in THF are used to calibrate the

molecular weight data. From Fig. C.1, multiple molecular weight modes can be identified for both sample oils, but slight differences in the overall molecular weight distribution are observed. For the CSB oil, two modes can be clearly distinguished as (i) a lower molecular weight component at $100\text{Da} \lesssim M \lesssim 1\text{kDa}$, corresponding to a base-oil phase with the number of carbon usually ranging from 15 to 40 [64], and (ii) a higher molecular weight component at $4\text{kDa} \lesssim M \lesssim 400\text{kDa}$, representing the macromolecular additives. For the M1 oil, the molecular weight distribution is more complicated with four major peaks marked by the red arrows. For both sample oils, more quantitative molecular weight distributions are obtained by decomposing and fitting the data of relative number concentration RC with a sum of logarithmic-normal (log-normal) distributions, or Wesslau distributions [65], which serve as a classical distribution for single-mode molecular weights. Based on the fit distributions, the number average molecular weight M_n and weight average molecular weight M_w can be calculated for each mode according to

$$M_n = \frac{\sum RC_i}{\sum RC_i/M_i}, \tag{C.1a}$$

$$M_w = \frac{\sum RC_i M_i}{\sum RC_i}, \tag{C.1b}$$

where M_i is the i-th molecular weight component, and RC_i stands for the normalized relative number concentration of component M_i. The number of chains of molecular weight i is proportional to RC_i/M_i. The results for both sample oils are listed in Table C.1. From this table, the larger values of the molecular weight ($M \gtrsim 1 - 10\text{kDa}$) can be connected to the additive phases, which provide a physical origin of the weakly non-Newtonian effects exhibited in the extensional rheology measured by our customized CaBER system. Deeper questions, such as how the molecular structure and quantity of the (unknown) additives affect the macroscopic rheology and the corresponding constitutive parameters (e.g. the magnitude of extensional thickening k_2 in the IRT model) are beyond the scope of the present study.

Table C.1: Results of the average molecular weights M_n, M_w and the polydispersity index (PDI) M_w/M_n from GPC results on the two sample oils. Each mode is quantitatively determined by fitting the RC data in Fig. C.1 into a sum of log-normal distributions.

Sample	Peak number	M_n [Da]	M_w [Da]	*PDI*
CSB	1	163	212	1.30
	2	27,173	63,305	2.33
M1	1	164	207	1.26
	2	321	335	1.04
	3	723	1,578	2.18
	4	38,617	59,292	1.54

Appendix D. Capillary thinning results on the filtered and unfiltered samples of CSB and M1 oils

To demonstrate the impact of macromolecular components on the rheological behaviors for both sample oils, we use PTFE filters (VWR International) to modify the molecular weight distributions of both samples. The pore
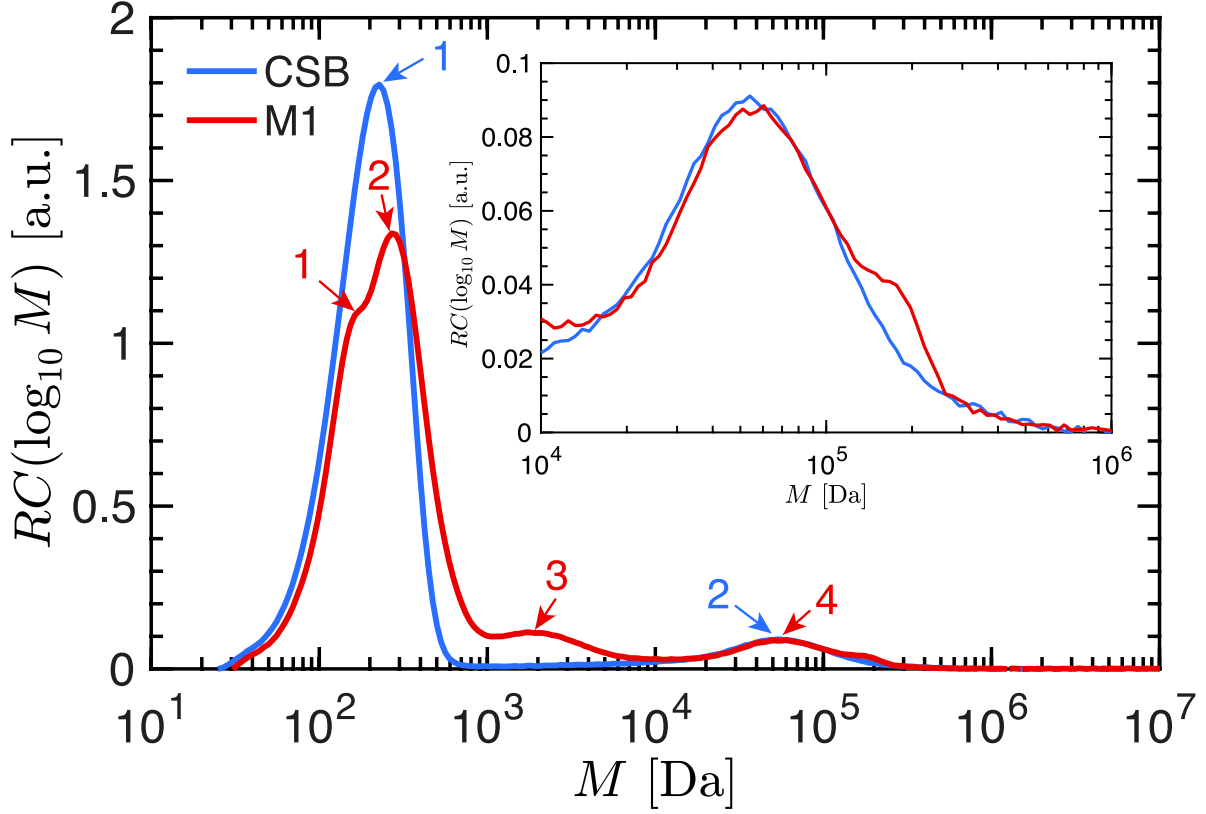
Figure C.1: GPC results of both sample oils, plotted as the relative number concentration (RC) against the molecular weight M. For both oils, tetrahydrofuran (THF) is used as the eluent at 30°C. The RC data are obtained from the RI detector of the GPC, and are further normalized. The molecular weight is calibrated from a series of monodisperse polystyrenes in THF at 30°C. From the figure, it is clear that both samples are polydisperse, comprised of multiple species that can be identified separately. For the CSB oil, two modes are identified: mode 1 is within the range $100\text{Da} \lesssim M \lesssim 1\text{kDa}$, and mode 2 is within the range $4\text{kDa} \lesssim M \lesssim 1000\text{kDa}$. For the M1 oil, four primary modes are identified, as labeled in the figure. The molecular weight of these motor oils can be quantitatively determined by fitting the RC data with a sum of log-normal distributions. For each mode, both M_n and M_w can be calculated using Eq. (C.1), and the results are shown in Table C.1. Inset: Relative number concentration at a higher molecular weight portion of $10\text{kDa} \leq M \leq 1000\text{kDa}$. For the M1 oil, a secondary peak can be seen at $M \approx 200\text{kDa}$.

size of the filter is carefully chosen as 450nm. From Appendix C, as well as the well-known Flory law relating the radius of gyration R_g with molecular weight [66], this size is selected to alter the macromolecular weight distribution while retaining the low molecular weight portion ($M \lesssim 10^4\text{Da}$). These filtered samples act as control samples to demonstrate the effects of different macromolecular components in the formulated oils on their extensional rheology. Capillary thinning experiments are performed on both unfiltered and filtered samples of each oil on the customized CaBER system. The same experimental setup is applied as shown in Table 2. The capillary thinning results are shown in Fig. D.1, and by using the best fitting model, we can extract the constitutive parameters as shown in Table D.1.

In Fig. D.1(a), both the unfiltered and filtered samples of the CSB oil are fit with the Oldroyd-B model. The results clearly show a decreased viscoelastic effect with the relaxation time changing from 5.37ms to 3.48ms (35.2% decrease). For the M1 oil, a similar result is observed in Fig. D.1(b). After filtration, the rate of extensional thickening
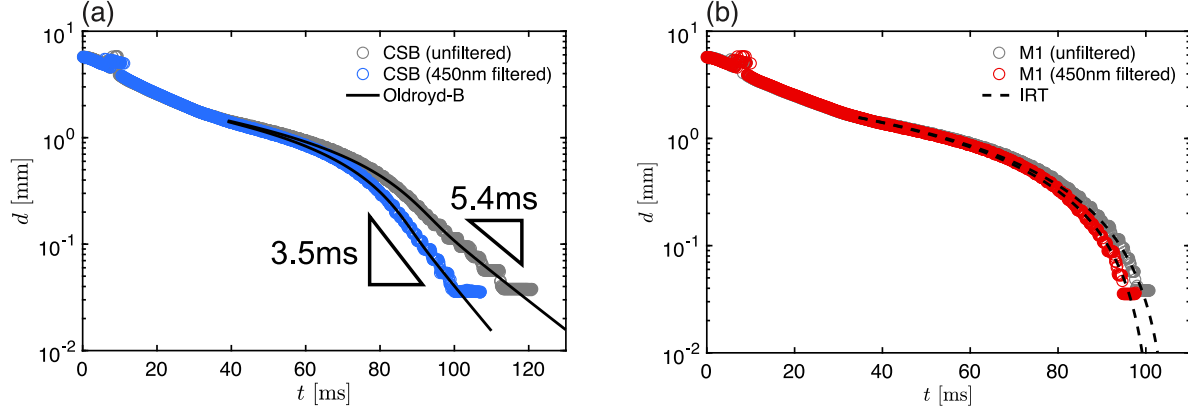
Figure D.1: Capillary thinning results on the unfiltered and filtered (pore size 450nm) samples of the two motor oils. The experimental setup is identical to Table 2, and we fit the capillary thinning dynamics of both samples with the best fit models. Compared with the capillary thinning dynamics of unfiltered samples, the samples after filtration show decreased viscoelasticity as parameterized by a decreased relaxation time (Oldroyd-B model) or rate of extensional thickening (IRT model).

Table D.1: Constitutive parameters extracted from the best fitting model for filtered (gray points) and filtered samples of each motor oil from their capillary thinning dynamics. (a) The CSB oil fit by the Oldroyd-B model. (b) The M1 oil fit by the IRT model. From the fitted constitutive parameters, both oils become less viscoelastic after filtration. This strongly suggests that the fluid viscoelasticity is likely to originate from the macromolecular components.

Model	Material	Parameters	Unfiltered	Filtered	Percentage of change
(a) Oldroyd-B	CSB	η_S [Pa $\cdot$ s]	0.258	0.220	-14.7%
		G [Pa]	8.12	14.79	$+82.1\%$
		λ [ms]	5.37	3.48	-35.2%
		Ec	11.3	8.6	-23.9%
(b) IRT	M1	η_0 [Pa $\cdot$ s]	0.244	0.242	-0.8%
		k_2 [Pa $\cdot$ s^2]	4.54×10^{-3}	3.67×10^{-3}	-19.2%
		Ec	3.6	3.2	-11.1%

k_2 is decreased from 4.54×10^{-3}Pa $\cdot$ s^2 to 3.67×10^{-3}Pa $\cdot$ s^2 (19.2% decrease). From Table D.1, we also note that the results from the unfiltered samples are consistent with Table 3, showing that the extensional rheological properties extracted from the customized CaBER system are highly repeatable.

The results of Fig. D.1 are worth some further discussion. The same pore size filter is applied to the two motor oils, which have a similar number average molecular weight M_n in the high molecular weight range ($M \geq 10^4$Da), as shown in Table C.1. However, the effectiveness of filtration can vary due to different macromolecular structures. As a result, the different degradation of viscoelasticity for the two sample oils shown in Fig. D.1 indicates that distinct macromolecular configurations or species can also result in different viscoelastic behavior. For the weakly elastic M1 oil, the high molecular components ($M \geq 10^4$Da) confer less nonlinear elasticity to the fluid than the additives used in the CSB oil. The resulting extensional rheology after filtration remains similar to that of an unfiltered sample. This observations are consistent with the M1 oil containing more rigid rod-like polymer chains or particulate additives. However, a more quantitative study connecting composition of the different oils to the ensuing extensional rheological

31

behavior is needed and will be left for future work.

References

[1] S. A. E. International, Engine oil viscosity classification, Tribology International 10 (2) (1977) 77–80. `doi: 10.1016/0301-679x(77)90102-5`.

[2] N. Canter, Special report: Additive challenges in meeting new automotive engine specifications, Tribology and Lubrication Technology 62 (9) (2006) 10–19.

[3] L. R. Rudnick, Lubricant additives: chemistry and applications, CRC Press, 2017.

[4] A. C. Eachus, It's not your father's motor oil, Tribology and Lubrication Technology 62 (6) (2006) 38.

[5] M. Smeeth, H. Spikes, S. Gunsel, Boundary film formation by viscosity index improvers, Tribology Transactions 39 (3) (1996) 726–734. `doi:10.1080/10402009608983590`.

[6] N. Canter, How does ZDDP function?, Tribology and Lubrication Technology 61 (6) (2005) 20–26.

[7] N. J. Mosey, T. K. Woo, Finite temperature structure and dynamics of zinc dialkyldithiophosphate wear inhibitors: A density functional theory and ab initio molecular dynamics study, Journal of Physical Chemistry A 107 (25) (2003) 5058–5070. `doi:10.1021/jp034085c`.

[8] N. J. Mosey, M. H. Müser, T. K. Woo, Molecular mechanisms for the functionality of lubricant additives, Science 307 (5715) (2005) 1612–1615. `doi:10.1126/science.1107895`.

[9] M. Ratoi, V. B. Niste, J. Zekonyte, WS2 nanoparticles-potential replacement for ZDDP and friction modifier additives, RSC Advances 4 (41) (2014) 21238–21245. `doi:10.1039/c4ra01795a`.

[10] N. Nunn, Z. Mahbooba, M. G. Ivanov, D. M. Ivanov, D. W. Brenner, O. Shenderova, Tribological properties of polyalphaolefin oil modified with nanocarbon additives, Diamond and Related Materials 54 (1) (2015) 97–102. `doi:10.1016/j.diamond.2014.09.003`.

[11] N. G. Demas, R. A. Erck, C. Lorenzo-Martin, O. O. Ajayi, G. R. Fenske, Experimental evaluation of oxide nanoparticles as friction and wear improvement additives in motor oil, Journal of Nanomaterials 2017 (2017) 8425782. `doi:10.1155/2017/8425782`.

[12] A. B. Vipper, Antioxidant properties of engine oil detergent additives, Lubrication Science 9 (1) (1996) 61–70. `doi:10.1002/ls.3010090103`.

[13] O. P. Parenago, A. B. Vipper, G. N. Kuz'mina, Zinc and molybdenum dithiocarbamates - antioxidant additives, Lubrication Science 13 (2) (2001) 113–124. `doi:10.1002/ls.3010130202`.

[14] S. Tarasov, A. Kolubaev, S. Belyaev, M. Lerner, F. Tepper, Study of friction reduction by nanocopper additives to motor oil, Wear 252 (1-2) (2002) 63–69. `doi:10.1016/S0043-1648(01)00860-2`.

[15] R. H. Johnson, W. A. Wright, The rheology of a multigraded motor oil, SAE Technical Papers (1968) 283–291`doi:10.4271/680072`.

[16] D. D. Joseph, K. Nguyen, G. S. Beavers, Non-uniqueness and stability of the configuration of flow of immiscible fluids with different viscosities, Journal of Fluid Mechanics 141 (1984) 319–345. `doi:10.1017/S0022112084000872`.

[17] M. F. Smith, J. P. Graham, Pumpability of multigrade engine oils at low temperature, Tech. rep., SAE Technical Paper (1971). `doi:10.4271/710139`.

[18] R. B. Bird, R. C. Armstrong, O. Hassager, Dynamics of Polymeric Liquids. Volume 1. Fluid Mechanics., 2nd Edition, Wiley-Interscience, 1987.

[19] J. Mewis, N. J. Wagner, Colloidal Suspension Rheology, Cambridge University Press, 2011. `doi:10.1017/CBO9780511977978`.

[20] J. F. Morris, A review of microstructure in concentrated suspensions and its implications for rheology and bulk flow, Rheologica Acta 48 (8) (2009) 909–923. `doi:10.1007/s00397-009-0352-1`.

[21] H. A. Barnes, Rheology of emulsions—a review, Colloids and Surfaces A: Physicochemical and Engineering Aspects 91 (1994) 89–95. `doi:doi.org/10.1016/0927-7757(93)02719-U`.

[22] C. Clasen, J. P. Plog, W.-M. Kulicke, M. Owens, C. Macosko, L. E. Scriven, M. Verani, G. H. McKinley, How dilute are dilute solutions in extensional flows?, Journal of Rheology 50 (6) (2006) 849–881. `doi:10.1122/1.2357595`.

[23] R. G. Larson, P. S. Desai, Modeling the rheology of polymer melts and solutions, Annual Review of Fluid Mechanics 47 (2015) 47–65. `doi:10.1146/annurev-fluid-010814-014612`.

[24] K. Ohsawa, S. Kiyama, Y. Nakamura, Y. Ochiai, S. Nakagawa, T. Oda, Y. Miyauchi, Visualization study on lubricant oil film behavior around piston skirt, Tech. rep., SAE Technical Paper (2011). `doi:10.4271/2011-01-2119`.

33

[25] G. H. McKinley, Visco-elasto-capillary thinning and break-up of complex fluids, Rheology Reviews 3 (2005) 1–48.
URL `http://hdl.handle.net/1721.1/18085`

[26] T. W. Bates, B. Williamson, J. A. Spearot, C. K. Murphy, Importance of oil elasticity, Industrial Lubrication and Tribology 40 (6) (1988) 4–19. `doi:10.1108/eb053384`.

[27] R. C. Coy, Practical applications of lubrication models in engines, Tribology International 31 (10) (1998) 563–571. `doi:10.1016/S0301-679X(98)00077-2`.

[28] A. V. Bazilevsky, V. M. Entov, A. N. Rozhkov, Liquid Filament Microrheometer and Some of Its Applications, in: Third European Rheology Conference and Golden Jubilee Meeting of the British Society of Rheology, Springer, 1990, pp. 41–43. `doi:10.1007/978-94-009-0781-2_21`.

[29] M. Renardy, A numerical study of the asymptotic evolution and breakup of Newtonian and viscoelastic jets, Journal of Non-Newtonian Fluid Mechanics 59 (2-3) (1995) 267–282. `doi:10.1016/0377-0257(95)01375-6`.

[30] G. H. McKinley, A. Tripathi, How to extract the Newtonian viscosity from capillary breakup measurements in a filament rheometer, Journal of Rheology 44 (3) (2000) 653–670. `doi:10.1122/1.551105`.

[31] P. K. Kundu, L. M. Cohen, Fluid Mechanics, 638 pp, Academic, Calif (1990).

[32] D. T. Papageorgiou, On the breakup of viscous liquid threads, Physics of Fluids 7 (7) (1995) 1529–1544. `doi:10.1063/1.868540`.

[33] K. Niedzwiedz, H. Buggisch, N. Willenbacher, Extensional rheology of concentrated emulsions as probed by capillary breakup elongational rheometry (CaBER), Rheologica Acta 49 (11) (2010) 1103–1116. `doi:10.1007/s00397-010-0477-2`.

[34] L. Martinie, H. Buggisch, N. Willenbacher, Apparent elongational yield stress of soft matter, Journal of Rheology 57 (2) (2013) 627–646. `doi:10.1122/1.4789785`.

[35] P. Moschopoulos, A. Syrakos, Y. Dimakopoulos, J. Tsamopoulos, Dynamics of viscoplastic filament stretching, Journal of Non-Newtonian Fluid Mechanics 284 (February) (2020) 104371. `doi:10.1016/j.jnnfm.2020.104371`.

[36] M. K. Tiwari, A. V. Bazilevsky, A. L. Yarin, C. M. Megaridis, Elongational and shear rheology of carbon nanotube suspensions, Rheologica Acta 48 (6) (2009) 597–609. `doi:10.1007/s00397-009-0354-z`.

[37] C. McIlroy, O. G. Harlen, Modelling capillary break-up of particulate suspensions, Physics of Fluids 26 (3) (2014) 33101. `doi:10.1063/1.4866789`.

[38] H. C.-H. Ng, A. Corker, E. García-Tuñón, R. J. Poole, GO CaBER: Capillary breakup and steady-shear experiments on aqueous graphene oxide (GO) suspensions, Journal of Rheology 64 (1) (2020) 81–93. `doi:` `10.1122/1.5109016.`

[39] P. Schümmer, K. H. Tebel, A new elongational rheometer for polymer solutions, Journal of Non-Newtonian Fluid Mechanics 12 (3) (1983) 331–347. `doi:10.1016/0377-0257(83)85006-X.`

[40] B. Keshavarz, V. Sharma, E. C. Houze, M. R. Koerner, J. R. Moore, P. M. Cotts, P. Threlfall-Holmes, G. H. McKinley, Studying the effects of elongational properties on atomization of weakly viscoelastic solutions using Rayleigh Ohnesorge Jetting Extensional Rheometry (ROJER), Journal of Non-Newtonian Fluid Mechanics 222 (2015) 171–189. `doi:10.1016/j.jnnfm.2014.11.004.`

[41] J. Dinic, Y. Zhang, L. N. Jimenez, V. Sharma, Extensional Relaxation Times of Dilute, Aqueous Polymer Solutions, ACS Macro Letters 4 (7) (2015) 804–808. `doi:10.1021/acsmacrolett.5b00393.`

[42] L. E. Rodd, T. P. Scott, J. J. Cooper-White, G. H. McKinley, Capillary break-up rheometry of low-viscosity elastic fluids, Applied Rheology 15 (1) (2005) 12–27. `doi:10.1515/arh-2005-0001.`

[43] L. Campo-Deaño, C. Clasen, The slow retraction method (SRM) for the determination of ultra-short relaxation times in capillary breakup extensional rheometry experiments, Journal of Non-Newtonian Fluid Mechanics 165 (23-24) (2010) 1688–1699. `doi:10.1016/j.jnnfm.2010.09.007.`

[44] J. Du, Rheological characterization of lubricants in automotive industries through development of a novel capillary breakup extensional rheometer, Master's thesis, Massachusetts Institute of Technology (2018).
URL `http://hdl.handle.net/1721.1/118729`

[45] V. M. Entov, E. J. Hinch, Effect of a spectrum of relaxation times on the capillary thinning of a filament of elastic liquid, Journal of Non-Newtonian Fluid Mechanics 72 (1) (1997) 31–53. `doi:10.1016/S0377-0257(97)` `00022-0.`

[46] V. Tirtaatmadja, T. Sridhar, Comparison of constitutive equations for polymer solutions in uniaxial extension, Journal of Rheology 39 (6) (1995) 1133–1160. `doi:10.1122/1.550632.`

[47] C. Wagner, L. Bourouiba, G. H. McKinley, An analytic solution for capillary thinning and breakup of FENE-P fluids, Journal of Non-Newtonian Fluid Mechanics 218 (2015) 53–61. `doi:10.1016/j.jnnfm.2015.01.011.`

[48] M. D. Torres, B. Hallmark, D. I. Wilson, L. Hilliou, Natural Giesekus fluids: Shear and extensional behavior of food gum solutions in the semidilute regime, AIChE Journal 60 (11) (2014) 3902–3915. `doi:10.1002/aic.` `14611.`

[49] B. Debbaut, M. J. Crochet, Extensional effects in complex flows, Journal of Non-Newtonian Fluid Mechanics 30 (2-3) (1988) 169–184. `doi:10.1016/0377-0257(88)85023-7`.

[50] H.-C. Tseng, A revisitation of generalized Newtonian fluids, Journal of Rheology 64 (3) (2020) 493–504. `doi:10.1122/1.5139198`.

[51] G. H. McKinley, T. Sridhar, Filament-stretching rheometry of complex fluids, Annual Review of Fluid Mechanics 34 (1) (2002) 375–415. `doi:10.1146/annurev.fluid.34.083001.125207`.

[52] A. Savitzky, M. J. Golay, Smoothing and Differentiation of Data by Simplified Least Squares Procedures, Analytical Chemistry 36 (8) (1964) 1627–1639. `doi:10.1021/ac60214a047`.

[53] D. C. Vadillo, W. Mathues, C. Clasen, Microsecond relaxation processes in shear and extensional flows of weakly elastic polymer solutions, Rheologica Acta 51 (8) (2012) 755–769. `doi:10.1007/s00397-012-0640-z`.

[54] V. Sharma, S. J. Haward, J. Serdy, B. Keshavarz, A. Soderlund, P. Threlfall-Holmes, G. H. McKinley, The rheology of aqueous solutions of ethyl hydroxy-ethyl cellulose (EHEC) and its hydrophobically modified analogue (hmEHEC): Extensional flow response in capillary break-up, jetting (ROJER) and in a cross-slot extensional rheometer, Soft Matter 11 (16) (2015) 3251–3270. `doi:10.1039/c4sm01661k`.

[55] D. M. Binding, An approximate analysis for contraction and converging flows, Journal of Non-Newtonian Fluid Mechanics 27 (2) (1988) 173–189. `doi:10.1016/0377-0257(88)85012-2`.

[56] S. L. Anna, G. H. McKinley, Elasto-capillary thinning and breakup of model elastic liquids, Journal of Rheology 45 (1) (2001) 115–138. `doi:10.1122/1.1332389`.

[57] J. Dinic, V. Sharma, Power Laws Dominate Shear and Extensional Rheology Response and Capillarity-Driven Pinching Dynamics of Entangled Hydroxyethyl Cellulose (HEC) Solutions, Macromolecules 53 (9) (2020) 3424–3437. `doi:10.1021/acs.macromol.0c00077`.

[58] J. Dinic, V. Sharma, Flexibility, Extensibility, and Ratio of Kuhn Length to Packing Length Govern the Pinching Dynamics, Coil-Stretch Transition, and Rheology of Polymer Solutions, Macromolecules 53 (12) (2020) 4821–4835. `doi:10.1021/acs.macromol.0c00076`.

[59] R. C. Armstrong, Kinetic theory and rheology of dilute solutions of flexible macromolecules. I. Steady state behavior, The Journal of Chemical Physics 60 (3) (1974) 724–728. `doi:10.1063/1.1681141`.

[60] K. A. Marshall, T. W. Walker, Investigating the dynamics of droplet breakup in a microfluidic cross-slot device for characterizing the extensional properties of weakly-viscoelastic fluids, Rheologica Acta 58 (9) (2019) 573–590. `doi:10.1007/s00397-019-01152-0`.

[61] J. Eggers, E. Villermaux, Physics of liquid jets, Reports on Progress in Physics 71 (3) (2008) 36601. `doi: 10.1088/0034-4885/71/3/036601`.

[62] M. L. Williams, R. F. Landel, J. D. Ferry, The Temperature Dependence of Relaxation Mechanisms in Amorphous Polymers and Other Glass-forming Liquids, Journal of the American Chemical Society 77 (14) (1955) 3701–3707. `doi:10.1021/ja01619a008`.

[63] J. C. Moore, Gel permeation chromatography. I. A new method for molecular weight distribution of high polymers, Journal of Polymer Science, Part A: Polymer Chemistry 34 (10) (1996) 1833–1841. `doi:10.1002/pola. 1996.842`.

[64] A. Sequeira, Lubricant Base Oil and Wax Processing, Marcel Dekker, New York, 1994.

[65] V. H. Weßlau, Die molekulargewichtsverteilung einiger niederdruckpolyäthylene, Die Makromolekulare Chemie 20 (1) (1956) 111–142. `doi:10.1002/macp.1956.020200109`.

[66] J. W. Kennedy, Principles of Polymer Chemistry, Vol. 76, Cornell University Press, 1954. `doi:10.1021/ ja01639a091`.